SOLUBILITY OF ROCK IN STEAM ATMOSPHERES OF PLANETS

BRUCE FEGLEY, JR.[1,2], NATHAN S. JACOBSON[3], K. B. WILLIAMS[2], J. M. C. PLANE[4], L. SCHAEFER[5], AND KATHARINA LODDERS[1,2]

[1] Planetary Chemistry Laboratory, McDonnell Center for the Space Sciences, Washington University, St. Louis, MO 63130, USA; bfegley@wustl.edu
[2] Department of Earth & Planetary Sciences, Washington University, St. Louis, MO 63130, USA
[3] Materials Division, NASA Glenn Research Center, MS106-1, 21000 Brookpark Road, Cleveland, OH 44135, USA
[4] School of Chemistry, University of Leeds, Leeds LS2 9JT, UK
[5] Harvard—Smithsonian Center for Astrophysics, 60 Garden Street, Cambridge, MA 02138, USA

ABSTRACT

Extensive experimental studies show that all major rock-forming elements (e.g., Si, Mg, Fe, Ca, Al, Na, K) dissolve in steam to a greater or lesser extent. We use these results to compute chemical equilibrium abundances of rocky-element-bearing gases in steam atmospheres equilibrated with silicate magma oceans. Rocky elements partition into steam atmospheres as volatile hydroxide gases (e.g., $Si(OH)_4$, $Mg(OH)_2$, $Fe(OH)_2$, $Ni(OH)_2$, $Al(OH)_3$, $Ca(OH)_2$, NaOH, KOH) and via reaction with HF and HCl as volatile halide gases (e.g., NaCl, KCl, CaFOH, CaClOH, $FAl(OH)_2$) in much larger amounts than expected from their vapor pressures over volatile-free solid or molten rock at high temperatures expected for steam atmospheres on the early Earth and hot rocky exoplanets. We quantitatively compute the extent of fractional vaporization by defining gas/magma distribution coefficients and show that Earth's subsolar Si/Mg ratio may be due to loss of a primordial steam atmosphere. We conclude that hot rocky exoplanets that are undergoing or have undergone escape of steam-bearing atmospheres may experience fractional vaporization and loss of Si, Mg, Fe, Ni, Al, Ca, Na, and K. This loss can modify their bulk composition, density, heat balance, and interior structure.

Key words: planets and satellites: atmospheres – planets and satellites: composition – planets and satellites: formation – planets and satellites: general – planets and satellites: terrestrial planets

1. INTRODUCTION

We investigated the solubility of rocky elements, in particular Mg, Si, and Fe in H_2O-rich (henceforth steam) atmospheres and the potential effects of their solubility for composition of hot rocky exoplanets and their atmospheres. Magnesium, silicon, and iron are the three most abundant elements in solar composition material that combine with oxygen to form rock (Lodders 2003). Their atomic abundances on the cosmochemical scale are similar to one another (within 20%) and are 1.03×10^6 (Mg), 1.00×10^6 (Si), and 0.848×10^6 (Fe). Other rock-forming elements that we also consider such as Al (0.0846×10^6), Ca (0.0604×10^6), Na (0.0577×10^6), Ni (0.049×10^6), and K (0.00376×10^6) are much less abundant, and we focus on Mg, Si, and Fe.

Oxygen, Mg, Si, and Fe are also the major elements in the silicate portions of meteorites, Earth (O + Mg + Si + Fe > 90% by mass), the other three terrestrial planets, and Earth's moon (see the geochemical analyses for meteorites, Earth, the Moon, Mars, and Venus in Lodders & Fegley 1998, and for Mercury in Nittler et al. 2011). Spectroscopic studies of main-sequence F and G stars with near-solar metallicity show constant ratios of Fe, Mg, and Si to one another (see Section 3.4.7 in Lodders et al. 2009). It is safe to assume that Mg, Si, and Fe are the most abundant rock-forming elements combined with oxygen in rocky exoplanets and the rocky cores of gas-rich and water-rich exoplanets around stars with solar or near-solar metallicity.

The solubility of Mg, Si, and Fe in steam atmospheres is significant. High-pressure steam in equilibrium with quartz + SiO_2—rich melt at 9.5–10 kbar and ~1080°C (the upper critical end point in the SiO_2–H_2O system) is ~50 mol% silica (Kennedy et al. 1962; Newton & Manning 2008), and molten $SiO_2 + H_2O$ are completely miscible at higher temperatures.

The significant solubility of Si and other rocky elements in steam (over a wide P–T range) raises interesting possibilities. One is the formation of *potentially* spectroscopically observable gases such as $Si(OH)_4$, $Mg(OH)_2$, $Fe(OH)_2$, $Ni(OH)_2$, $Al(OH)_3$, $Ca(OH)_2$, NaOH, and KOH and their photolysis products. Another is loss of Mg, Si, Fe, Ni, Al, Ca, Na, and K from hot rocky exoplanets that are losing or have lost steam-bearing atmospheres. Significant changes in the relative ratios of Mg, Si, Fe, and Ni may alter the bulk composition, density, and interior structure of the remnant rocky planet left after loss of an early-formed steam atmosphere. The loss of radioactive ^{40}K may also affect the heat balance of a remnant rocky planet. The loss of Si, Al, Ca, Na, and K—abundant in Earth's continental crust—may alter the surface composition, mineralogy, and structure of a remnant rocky planet.

Our work is motivated by three disparate developments: (1) observations of over 100 hot rocky exoplanets in recent years, (2) theoretical models of steam atmospheres on the early Earth and rocky exoplanets, and (3) experimental measurements of the solubility of minerals and rocks in steam.

Nearly all of the known hot rocky exoplanets are closer to their host stars than Mercury is to the Sun. All small exoplanets ($R < 2.7 R_{Earth}$) with well-constrained masses (as of 2015 December) receive at least 10 times more stellar insolation than Earth (e.g., Figure 13 of Gettel et al. 2015), with correspondingly higher equilibrium temperatures. The hottest of these are planets such as CoRoT-7b and Kepler-10b, with equilibrium temperatures greater than 2000 K. However, others, such as the newly discovered MEarth planet GJ 1132 b (Berta-Thompson et al. 2015) and the closest and brightest transiting super-Earth HD 219134 b (Motalebi et al. 2015), have lower temperatures of 500 and 1100 K, respectively. Many of the hot rocky exoplanets lie on a density curve consistent with the composition of Earth (Dressing et al. 2015). However, this

population of planets ($R < 2.7\,R_{Earth}$) also includes objects with densities low enough to require substantial volatile envelopes on top of their solid (or liquid) surface. These include 55 Cancri e, Kepler-454 b, Kepler-11b, Kepler 48-c, HIP 116454b, HD 97658b, and Kepler-10c, which have equilibrium temperatures ranging from ~600 K to greater than 2000 K. New planets in this radius range are being discovered rapidly with K2 (e.g., Vanderburg et al. 2015), and even more planets in short-period orbits will probably be discovered following the launches of the *Transiting Exoplanet Survey Satellite* mission and the *CHaracterizing ExOPlanet Satellite* (*CHEOPS*) mission in 2017. The *James Webb Space Telescope*, slated for launch in 2018, should be able to take detailed infrared spectra of these planets' atmospheres.

The planets discussed above are important here because, given their high temperatures and an Earth-like volatile abundance, they could have a steam atmosphere that would generate surface temperatures hot enough to melt silicates. For comparison, (water-poor) Venus has an equilibrium temperature of ~260 K, but its atmosphere of ~95 bars of CO_2 (with much smaller amounts of SO_2 and H_2O) produces surface temperatures of ~740 K. Venus's surface is almost hot enough to melt alkali-rich silicates, e.g., the albite—sodium disilicate eutectic is 767 K (Table 12-1 in Fegley 2013), and all of the planets mentioned above have significantly higher equilibrium temperatures than Venus. Although steam atmosphere conditions on Earth were likely transient, the lifetime of potential steam atmospheres on the hot rocky exoplanets would be limited only by atmospheric escape. Hydrodynamic escape of hydrogen can also drag along heavier elements—up to Xe—if the outflow is strong enough (e.g., Hunten et al. 1987; Pepin 1997). Therefore, the solubility of rocky elements in steam may lead to elemental fractionation on planets with long-lived steam atmospheres undergoing escape. However, we stress that our chemical equilibrium calculations are not tied to any particular planet mentioned above, but are meant to map out atmospheric chemistry across a wide *P, T* range.

Our previous models were about outgassing during planetary accretion and atmospheric chemistry of rocky planets in our solar system and other planetary systems and used chemical equilibrium and chemical kinetic calculations. Schaefer & Fegley (2007, 2010) modeled the composition of the major volatile-bearing gases (H, C, N, O, S) in outgassed atmospheres as functions of temperature and total pressure for the different types of chondritic material (i.e., carbonaceous [CI, CM, CV], ordinary [H, L, LL], and enstatite [EH, EL]). Schaefer & Fegley (2009) did chemical equilibrium models of silicate vapor atmospheres on volatile-free hot rocky exoplanets such as CoRoT-7b. Schaefer et al. (2012) considered vaporization of volatile-bearing hot rocky exoplanets like Earth using two rocky compositions—Earth's SiO_2-rich continental crust and the MgO- and FeO-rich bulk silicate Earth (BSE). The BSE is the composition of Earth's silicate portion before it evolved into the atmosphere, oceans, crust, and mantle. It has a mass of 4.03×10^{24} kg, of which the mantle is 99.4%, so the BSE composition is close to that of Earth's mantle.

Outgassing of the two model compositions generated atmospheres rich in steam and CO_2 with variable amounts of other gases depending on pressure and temperature (e.g., see Figures 1–5, and Table 3 in Schaefer et al. 2012). The major Mg, Si, and Fe gases in their 100 bar model were $Mg(OH)_2$, SiO, and $Fe(OH)_2$.

At the time the calculations in Schaefer et al. (2012) were done, a thorough assessment of the thermodynamics of SiO_2 solubility in steam and the derived thermodynamic properties of $Si(OH)_4$ gas was unavailable. Fegley (2014) used the recently published $Si(OH)_4$ data of Plyasunov (2011b, 2012) and found $Si(OH)_4$ partial pressures 10,000 times larger than the SiO partial pressure expected from Si vaporization from anhydrous lavas at the same conditions (BSE-like melt at 1873 K in a 100 bar H_2O–CO_2 atmosphere). This preliminary result warrants more comprehensive models of rocky element solubility in steam atmospheres.

This paper is organized as follows. Section 2 briefly reviews the history of prior work on steam atmosphere models, describes effects of steam atmospheres on rock melting, and discusses the size of steam atmospheres expected from the current H_2O and CO_2 content of Earth's mantle for the early Earth. Section 3 reviews prior experimental and theoretical studies on the solubility of rock-forming elements in steam and focuses on Si, the rocky element that is the most soluble in steam.

Section 4 describes the methods used in our chemical equilibrium calculations. Section 5 compares the solubility of Mg, Si, Fe, Ni, Al, and Ca in steam to the vapor pressure of the pure oxides. Section 6 demonstrates that other gases possibly present in steam atmospheres (CO_2, N_2, SO_2, O_2, and CH_4) are inert dilutants that do not alter the solubility of Mg, Si, and Fe in steam.

Section 7 describes the results of our chemical equilibrium calculations of metal hydroxide gas abundances in steam atmospheres of hot rocky exoplanets. These calculations take into account chemical interactions with magma oceans on these planets. (We use the terms "rocky elements" and "metals" interchangeably.) The effects of fractional vaporization of rocky elements on the bulk composition of the residual planet are illustrated in several figures and tabulated using gas/ magma distribution (i.e., partition) coefficients. We show that the Si/Mg ratio in the BSE can be produced by loss of a steam atmosphere with a few percent of the BSE mass. Section 7 also describes the effects of stellar UV photolysis on abundances of the major hydroxide gases of Mg, Si, and Fe and lists some gases that may be observable spectroscopically. Section 8 discusses some cosmochemical applications of our work and suggests some future avenues. Section 9 summarizes our major conclusions.

2. STEAM ATMOSPHERES

2.1. Historical Review

Arrhenius et al. (1974) proposed that heating during accretion of Earth degassed water-bearing minerals in the accreted planetesimals and formed a steam atmosphere. The steam atmosphere formed Earth's hydrosphere as Earth cooled, a process that may have taken ~2.5 Myr (Sleep et al. 2001). Subsequent experiments showed that water and CO_2 are the two major volatiles formed by impact degassing of CM2 carbonaceous chondritic material during planetary accretion (e.g., Lange & Ahrens 1982; Tyburczy et al. 1986). Chemical equilibrium calculations showed that H_2O and CO_2 are the two major gases formed by impact degassing of CI, CM2, and CV3 chondritic material (Schaefer & Fegley 2010). Theoretical models of the origin and evolution of an impact-generated

steam atmosphere on the early Earth were presented by Abe & Matsui (e.g., Abe & Matsui 1985, 1988; Matsui & Abe 1986).

Fegley & Schaefer (2014) modeled a massive (~1000 bar) H_2O–CO_2–SO_2 steam atmosphere on the early Earth and computed gas-phase chemical equilibria in it from 2000 to 6000 K. They found that thermal dissociation of H_2O, CO_2, and SO_2 produced increasing amounts of OH, H_2, CO, O_2, H, O, and SO with increasing temperature at constant total pressure (see their Figure 5). They also showed that a steam atmosphere was significantly more oxidizing with a higher oxygen fugacity (fO_2) than the solar nebula and suggested that easily oxidized elements such as Si, Fe, Cr, Mo, W, B, and V would vaporize from the magma ocean as hydroxides (e.g., $Si(OH)_4$, $Fe(OH)_2$, H_2CrO_4, H_2MoO_4, H_2WO_4, H_3BO_3) and gaseous oxides of Cr, Mo, V, and W. This is potentially important for the early Earth because geochemical signatures may be in the rock record (B. Fegley et al. 2016, in preparation).

2.2. Effects on Rock Melting

Water vapor and CO_2 are greenhouse gases, and the development of a massive steam atmosphere and a magma ocean at the planetary surface are closely linked (e.g., Abe & Matsui 1985, 1988; Matsui & Abe 1986; Zahnle et al. 1988; Abe 1993; Elkins-Tanton 2008; LeBrun et al. 2013). A sufficiently massive steam atmosphere can heat the surface of a rocky planet to (and above) the melting point of rock (e.g., see the discussion in Zahnle et al. 1988).

At 1 bar pressure peridotite, the major rock in Earth's upper mantle, starts to melt at 1120–1200°C (1390–1473 K, the solidus, T_{sol}) and is completely molten by ~1970 K (the liquidus, T_{liq}) (e.g., see Kushiro et al. 1968; Takahashi 1986; Takahashi et al. 1993). The bulk composition of peridotite rock from different locales, in particular the Na/Ca ratio, alters the solidus temperature (Green 2015). Peridotite melting has a positive Clapeyron slope dT_{sol}/dP of ~12 K kbar^{-1} (120 K GPa^{-1}) in the 1 bar–50 kbar range (Kushiro et al. 1968; Green 2015), and the increased pressure caused by the weight of a massive steam atmosphere will increase the melting point. However, this is counteracted by the freezing point depression due to the solubility of H_2O (more soluble) and CO_2 (less soluble) in silicate magmas. The negative ΔT from the freezing point depression is larger than the positive ΔT from the increased pressure, and the net effect is that the melting point of H_2O-saturated peridotite is less than that of dry peridotite, by about 400°C at 26 kbar pressure (≈80 km depth; see Figure 1 in Kushiro et al. 1968). Dissolution of H_2O and CO_2 also lowers the freezing points of other molten rocks and minerals and is a general effect that is expected to occur on any rocky exoplanet made of silicates that also contains CO_2 and water.

2.3. Steam Atmosphere on the Early Earth

The properties (e.g., mass, composition, lifetime) of a steam atmosphere on a planet depend on several factors, such as the total amount of water and other volatiles, the fractional amount of the volatiles that are outgassed into the atmosphere, planetary surface temperature, planetary distance from the primary star, and primary star type (e.g., see Hamano et al. 2013, 2015). For illustration we briefly discuss possible properties of a steam atmosphere on early Earth.

The mass fraction (in ppm = parts per million) of hydrogen in the BSE is 120 ppm (~1070 ppm as H_2O) (Palme & O'Neill 2014). This mass fraction of H_2O is equivalent to ~4.3 × 10^{21} kg of water versus ~1.7 × 10^{21} kg of H_2O in the hydrosphere (oceans + glaciers + freshwater). Thus, only about 40% of Earth's total water is outgassed on its surface, and additional water ~1.6 times that in the hydrosphere remains inside the BSE. Other estimates of water in the BSE are smaller, but they still give about one hydrosphere worth of water inside Earth (Saal et al. 2002; Hirschmann & Dasgupta 2009).

Palme and O'Neill (2014) list 100 ppm carbon (~370 ppm as CO_2) in the BSE. Other estimates for the carbon content of the BSE range from 46 to 250 ppm (summarized in Table 6.9 of Lodders & Fegley 1998). Using the Palme & O'Neill (2014) values, mass balance shows that outgassing of all hydrogen and carbon in the BSE as H_2O (4.3 × 10^{21} kg) and CO_2 (1.5 × 10^{21} kg) would give a steam atmosphere with a surface pressure of ~1100 bar composed of ~75% steam and 25% CO_2 (P = mg, using g = 980.665 cgs). LeBrun et al. (2013) consider a similar range of 100–1000 bars for a steam—CO_2 atmosphere on the early Earth.

This calculation is illustrative and assumes that the silicate portion of the early Earth had the same composition and mass as the BSE and current surface gravity. Earth's volatile depletion with respect to chondritic material and solar abundances suggests that all estimates of its current volatile content are plausibly smaller than its initial endowment (e.g., see pp. 73–77 in Fegley & Schaefer 2014). Although the exact properties of steam atmospheres on the early Earth and hot rocky exoplanets depend on several variables, we explicitly assume that steam atmospheres form and we explore their effect on chemistry of rock-forming elements with an emphasis on the major elements Si, Mg, and Fe.

3. PAST WORK ON THE SOLUBILITY OF ROCKY ELEMENTS IN STEAM

Extensive experimental work going back to the 1930s shows that most elements found in rocks are soluble in steam (e.g., see Alexander et al. 1963; Maeda et al. 1978; Hashimoto 1992 for MgO; Antignano & Manning 2008; Nguyen et al. 2014 for TiO_2; Belton & Richardson 1962; Belton & Jordan 1967 for Co, Fe, Ni; Matsumoto & Sata 1981; Hashimoto 1992 for CaO; Hashimoto 1992; Opila & Myers 2004 for Al_2O_3; Meschter et al. 2013 for a review of all elements; Morey 1957 for Al_2O_3, $BaSO_4$, BeO, $CaCO_3$, $CaSO_4$, Fe_2O_3, GeO_2, NaCl, Na_2SO_4, Nb_2O_5, NiO, $PbSO_4$, SiO_2, SnO_2, Ta_2O_5, and ZnS; Preston & Turner 1934; Van Nieuwenberg & Blumendal 1930, 1931a, 1931b for SiO_2; Verhoogen 1949, p. 91; Shen & Keppler 1997; Bureau & Keppler 1999 for several minerals). In order of decreasing solar elemental abundances (Lodders 2003), this list of rock-forming elements includes Mg, Si, Fe, Al, Ca, Na, Ni, Cr, Mn, P, K, Ti, Co, Zn, V, Li, Ga, Sr, B, Zr, Rb, Te, Y, Ba, Mo, La (and other rare Earth elements), Cs, Be, W, and U.

The geological literature contains many experimental studies of the solubility of silica in water, steam, and mixtures of the two and empirical models for total silica solubility because of its importance for processes in Earth's crust and mantle (e.g., Kennedy 1950; Morey & Hesselgesser 1951a, 1951b; Morey 1957; Kitahara 1960; Kennedy et al. 1962; Morey et al. 1962; Weill & Fyfe 1964; Anderson & Burnham 1965; Walther & Helgeson 1977; Fournier & Potter 1982; Manning 1994;

Rimstidt 1997; Gunnarsson & Arnórsson 2000; Newton & Manning 2002, 2003, 2008; Hunt & Manning 2012; Cruz & Manning 2015).

Although significant dissolution of silica in steam was recognized early, the molecular form(s) of the Si-bearing gas (es) in steam remained unknown until Brady (1953) analyzed experimental data of Kennedy (1950), Morey & Hesselgesser (1951a, 1951b), and Straub & Grabowski (1945). Brady inferred that orthosilicic acid vapor $Si(OH)_4$ is the major Si-bearing molecule in steam over a wide P–T range. Subsequent work supports his conclusions (e.g., see Mosebach 1957; Wasserburg 1958; Kitahara 1960; Krikorian 1970; Walther & Helgeson 1977; Hashimoto 1992; Zotov & Keppler 2002; Jacobson et al. 2005; Plyasunov 2011b, 2012 and references therein). Silica dissolves in steam primarily via the reaction

$$SiO_2(silica) + 2H_2O(steam) = Si(OH)_4(gas). \quad (1)$$
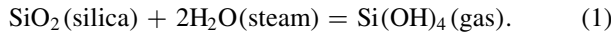
In particular, we refer the reader to Plyasunov (2011b, 2012). He carefully analyzed ambient pressure transpiration experiments, solubility data for amorphous silica and quartz in water—steam mixtures along the H_2O vapor pressure curve up to the critical point of water (647.096 K), and in steam above the critical point. He computed ideal gas thermodynamic properties and fugacity coefficients for $Si(OH)_4$ gas, partition coefficients for $Si(OH)_4$ between water and steam, and showed that reaction (1) accounts for 100% of dissolved silica in steam at densities $\leqslant 322$ kg m^{-3}, the density of H_2O at its critical point (e.g., see Table 3 and Figures 7, 9, and 14 in Plyasunov 2012).

4. COMPUTATIONAL METHODS AND DATA SOURCES

We performed three different sets of calculations: (1) the estimated partial pressures of $Si(OH)_4$ and other Si–O–H gases in steam as a function of P and T from 1573 to 2000 K and from 4×10^{-5} to 1100 bars, (2) the solubility of pure oxides (SiO_2, MgO, "FeO," CaO, Al_2O_3, NiO) in steam, and (3) the chemistry of a steam atmosphere in equilibrium with a magma ocean. The first set of calculations confirms that $Si(OH)_4$ is the major Si-bearing gas in steam at high temperatures up to 1100 bars of pressure, in agreement with the prior experimental and theoretical work cited above. It also shows agreement between calculations performed with the IVTAN code at Washington University and with the FactSage code at NASA Glenn. The second set shows the maximum solubility of an oxide in steam and the maximum pressure of the respective hydroxide gas as a function of temperature and steam pressure. The third set of calculations gives the abundances of metal hydroxide gases in the steam atmosphere of an exoplanet. Gas abundances are expressed as mole fractions (X) defined as moles (N) of a gas divided by total moles of all gases in the atmosphere

$$X_i = \frac{N_i}{\sum_{i=1}^{i=N} N_i}. \quad (2)$$

We used the IVTAN code, which is a Gibbs-energy minimization code of the type described by Van Zeggern & Storey (1970), to perform ideal gas and real gas chemical equilibrium calculations. Thermodynamic data are from the NIST-JANAF Tables (Chase 1998), the IVTAN database (Gurvich et al. 1983, 1989), Robie & Hemingway (1995), and other sources cited in the text below. Several hundred compounds of the elements discussed in this paper were included in the chemical equilibrium calculations.

Our first set of calculations (discussed in Section 5.1) uses experimental data for $Si(OH)_4$ gas from Plyasunov (2011b, 2012) and estimated thermodynamic data for other Si–O–H gases from Krikorian (1970) and Allendorf et al. (1995). Krikorian (1970) estimated molecular geometry, bond lengths, and vibrational frequencies for Si–O–H gases by analogy with related compounds and used statistical mechanics (Pitzer & Brewer 1961, chapter 27) to compute free energy functions $[(G^o_T - H^o_0)/T]$. He computed standard enthalpy of reaction values at 0 K from his analysis of data for SiO_2 solubility in steam. The combination of the two functions gives the standard Gibbs energy for formation of an ideal gas at 1 bar pressure from its constituent elements in their reference states as a function of temperature via the relationship

$$\frac{\triangle G^o_T}{T} = \triangle \left[\frac{(G^o_T - H^o_0)}{T} \right] + \frac{\triangle H^o_0}{T}. \quad (3)$$

For example, the standard Gibbs energy for formation of $Si_2O(OH)_6$ gas is the Gibbs energy change for the reaction

$$2Si(crystal) + 7/2O_2(gas) + 3H_2(gas) = Si_2O(OH)_6(gas). \quad (4)$$
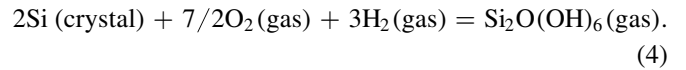
The change in the Gibbs energy functions for this reaction is

$$\triangle \left[\frac{(G^o_T - H^o_0)}{T} \right]$$
$$= \left[\frac{(G^o_T - H^o_0)}{T} \right]_{Si_2O(OH)_6} - 2 \left[\frac{(G^o_T - H^o_0)}{T} \right]_{Si(c)}$$
$$- \frac{7}{2} \left[\frac{(G^o_T - H^o_0)}{T} \right]_{O_2(g)} - 3 \left[\frac{(G^o_T - H^o_0)}{T} \right]_{H_2(g)}. \quad (5)$$

In contrast, Allendorf et al. (1995) used quantum chemistry composite calculations to compute molecular geometry and vibrational frequencies for Si–O–H gases and then used statistical mechanics to compute Gibbs energy functions for Si–O–H gases. Allendorf et al. (1995) computed standard enthalpy of formation values from their quantum chemistry calculations. They then computed the temperature-dependent ΔG^o_T value for a gas using the same equations shown above.

The interactions of $Si(OH)_4$ and the other metal hydroxide gases with H_2O are strongly non-ideal at some P, T conditions, and we used fugacity coefficients (ϕ) for H_2O, $Si(OH)_4$, $Mg(OH)_2$, $Fe(OH)_2$, $Ca(OH)_2$, $Ni(OH)_2$, and $Al(OH)_3$ in our real gas calculations. The fugacity coefficients for H_2O were calculated from the equation of state (EOS) for water using the LonerHGK code (Bakker 2009) available from his Web site (fluids.unileoben.ac.at). Figures 1 and 2 illustrate the extent of non-ideality for H_2O and $Si(OH)_4$ at pressures $\leqslant 2000$ bar, where our calculations were performed.

Plyasunov (2011a, 2012) used the truncated virial EOS to derive fugacity coefficients for $B(OH)_3$ and $Si(OH)_4$ in steam. His modeling shows

$$\frac{\ln_2^\infty}{\ln_1^*} = \frac{2B_{12}}{B_{11}} - 1 = k. \quad (6)$$

The k is an empirical constant, which equals 6.8 ± 0.4 (2σ) for $Si(OH)_4$ and 5.2 ± 0.30 (2σ) for $B(OH)_3$; the fugacity coefficient and second virial coefficient for pure steam are ϕ_1^* and B_{11}, respectively; the fugacity coefficient for the second component at infinite dilution in steam is ϕ_2^∞; and the second
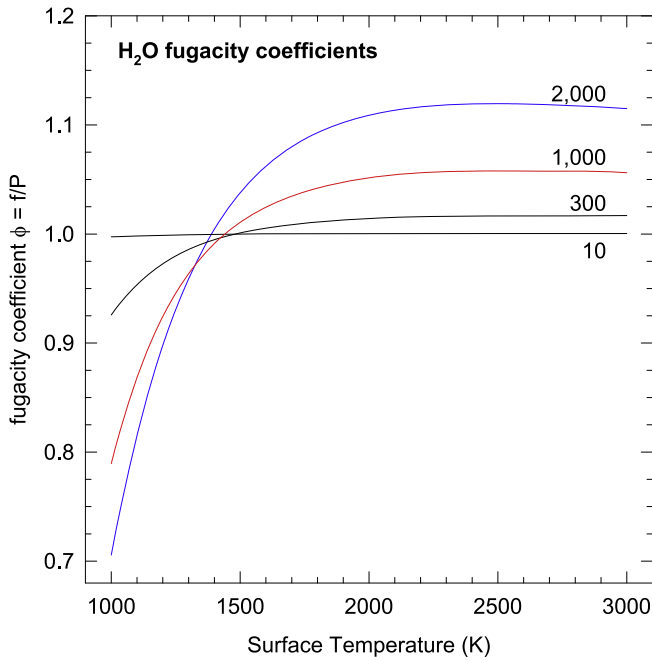
Figure 1. Fugacity coefficient ($\phi = f/P$) isobars for steam from 1000 to 3000 K. The ϕ values are unity within 0.5% at 10 bars and within 0.02% at $P <$ 10 bars and are calculated from the EOS for water using the Loner HGK code of Bakker (2009). Compare the ordinate in this graph with that in Figure 2.
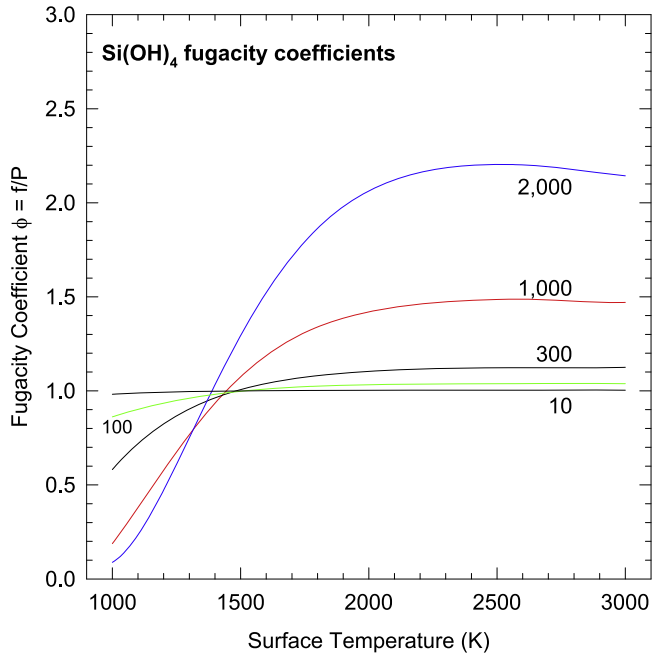
Figure 2. Fugacity coefficient ($\phi = f/P$) isobars for Si(OH)$_4$ from 1000 to 3000 K. The ϕ values are calculated as described by Akinfiev & Plyasunov (2013). Compare the ordinate in this graph with that in Figure 1.

cross virial coefficient for the second component is B_{12}. Plyasunov (2011a, 2012) showed that the infinite dilution approximation is valid over a wide P, T range for the dilute solutions of B(OH)$_3$ and Si(OH)$_4$ in steam. Based on his modeling, Akinfiev & Plyasunov (2013) propose that the empirical constant k for a molecule MO$_n$(OH)$_p$(H$_2$O)$_q$ is given

by the formula

$$k = 2(n + p + q) - 1. \qquad (7)$$

This formula gives $k = 7$ for Si(OH)$_4$ versus the observed value of 6.8 ± 0.4 and $k = 5$ versus the observed value of 5.2 ± 0.30 for B(OH)$_3$ gas. The dihydroxide gases of Ca, Fe, Mg, and Ni have $k = 3$. The pressure range in Figure 2 corresponds to the density range in which Plyasunov's fugacity coefficients for Si(OH)$_4$ are valid (see Table 3 and Figures 7, 9, and 14 in Plyasunov 2012).

We considered the effect of pressure on condensed phases for our calculations of oxide solubility in steam, i.e., the contribution of the VdP term to Gibbs energy in the fundamental equation (dG = VdP − SdT). This is often discussed in terms of thermodynamic activity, "a." At 1 bar pressure the thermodynamic activity of pure condensed phases, such as quartz or molten silica, is unity. However, pressures greater than 1 bar increase the thermodynamic activity of condensed phases. Using quartz as an example, its activity (a) at higher pressure is given by the thermodynamic relationship (e.g., see pp. 474–476 in Fegley 2013)

$$RT \ln a = \int_1^P V(T, P) dP. \qquad (8)$$

This is a perfectly general equation. We evaluated it using the equation

$$V(T, P) = V_{298}^o [1 + \alpha_P(T - 298) - \beta_T(P - 1)]. \qquad (9)$$

The $V^o{}_{298}$ is the molar volume of quartz at 298 K and the standard state pressure of 1 bar, and $V(T, P)$ is the temperature-dependent (and pressure-dependent) molar volume of quartz. The units of molar volume are J bar^{-1} mol^{-1}, R is the ideal gas constant ($R = 8.3145$ J bar^{-1} K^{-1} mol^{-1}), T is Kelvin temperature, and P is pressure in bars. The isobaric thermal expansion coefficient α_P (K^{-1}) (e.g., see pp. 33–34 in Fegley 2013) is

$$\alpha_P = \frac{1}{V}\left(\frac{\partial V}{\partial T}\right)_P = \left(\frac{\partial lnV}{\partial T}\right)_P. \qquad (10)$$

The isothermal compressibility coefficient (β_T bar^{-1}) (e.g., see pp. 34–35 in Fegley 2013) is defined as

$$\beta_T = -\frac{1}{V}\left(\frac{\partial V}{\partial P}\right)_T = -\left(\frac{\partial lnV}{\partial P}\right)_T = \frac{1}{K}. \qquad (11)$$

The K in this equation is the isothermal bulk modulus. Hemingway et al. (1998) give the molar volume, isobaric thermal expansion coefficient (a_P) for quartz, and isothermal compressibility as $V^o{}_{298} = 2.269$ J bar^{-1} mol^{-1},

$$\alpha_P = 4.48 \times 10^{-5} + 6.3 \times 10^{-9}(T - 298), \qquad (12)$$

and $\beta_T = 2.7 \times 10^{-6}$ bar^{-1}, respectively. We used analogous equations to compute activity as a function of pressure for the stable silica polymorph at ambient temperature (quartz, cristobalite, molten SiO$_2$) and the other solid and liquid oxides we considered. The input data are from Holland & Powell (2011), Fei & Ahrens (1995), and Linard et al. (2008).

Within its calibration range, the MELTS code (described next) incorporates the effect of pressure on activity, and no further calculations were necessary for oxide activities in the silicate magmas for the continental crust and BSE.

We used the pMELTS (version 5.6.1) and rhyolite-MELTS (version 1.02) codes (Ghiorso & Sack 1995; Ghiorso et al. 2002; Gualda et al. 2012) to calculate the activities of rock-forming oxides for both the BSE and continental crust compositions. The activity of an oxide is proportional to its mole fraction (X) in the melt ($a = \gamma \cdot X$), and the proportionality constant is the activity coefficient (γ). The calculated activities were input into the IVTAN code along with the compositions of the BSE (or continental crust) and fugacity coefficients for H_2O and the metal hydroxide gases to model chemical equilibria between the steam atmosphere and magma ocean. The MELTS programs are Gibbs energy minimization codes using regular solution models for silicate liquids and coexisting mineral phases as a function of temperature, pressure, and oxygen fugacity. In some runs we set the oxygen fugacity (f O_2) equal to that of the steam atmosphere by varying the Fe^{2+}/Fe^{3+} ratio of the starting composition at each temperature step. The MELTS program gives activities of selected mineral components in the melt (e.g., Si_4O_8, Mg_2SiO_4, Fe_2SiO_4, Al_4O_6, $Ca_2Si_2O_6$, $NiSi_{0.5}O_2$, $NaSi_{0.5}O_{1.5}$, $KAlSiO_4$). Carmichael et al. (1977) and Ghiorso & Carmichael (1980) discuss the reasons for using mineral instead of oxide components. Using thermodynamic data from Berman (1988) and Robie & Hemingway (1995), we converted activities of the molten mineral components used in the MELTS program to activities of molten oxides of interest (SiO_2, Al_2O_3, MgO, FeO, CaO, Na_2O, K_2O, NiO).

We compared results of the MELTS programs with the FactSage code, which is a Gibbs energy minimization code that uses the quasi-chemical model to describe thermodynamic properties of multicomponent oxide melts. FactSage has been extensively tested and validated against experimental data, but it is generally optimized for molten oxide systems important in metallurgy and materials science (Bale et al. 2002). There is generally good agreement with results from the MELTS and FactSage codes as subsequently mentioned throughout the paper.

In response to a question by the referee about whether we are assuming only oxides in the magma—which we think other readers may share—we comment briefly on thermodynamic modeling of molten oxides and silicates (i.e., the magma ocean). Molten silicates conduct electricity and are ionic in nature (e.g., see the classic work of Bockris et al. 1948, 1952a, 1952b). However, thermodynamic data are unavailable for the actual ionic species in the melts. Fortunately, thermodynamic modeling of solutions (molten silicates in this case) does not have to use the actual species present in the solutions, and any choice of components can be made. In their discussion of components and solutions, Pitzer & Brewer (1961) noted, "The components are the substances of fixed composition which can be mixed in varying amounts to form the solution. For thermodynamic purposes, the choice of components of a system is often arbitrary and depends on the range of conditions for the problem being considered." The two codes we used chose molten minerals (MELTS) or molten oxides (FactSage) as components for their melt models. A series of papers by developers of the two codes (e.g., Blander & Pelton 1984; Pelton & Blander 1984; Ghiorso & Sack 1995; Ghiorso et al. 2002; Gualda et al. 2012) show how closely the two codes reproduce experimental measurements for molten silicates. We discuss our results in terms of the activities of oxides in the magma ocean, but this does not necessarily mean

that SiO_2, MgO, FeO, and so on are the actual species present. In some cases the use of negative amounts of components is advantageous for thermodynamic models of solid solution in mica and amphibole minerals (Korzhinskii 1959; Thompson 1981). A simple example illustrating use of negative components is given by Fegley (2013, pp. 236–237).
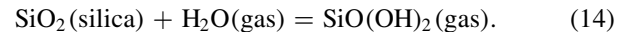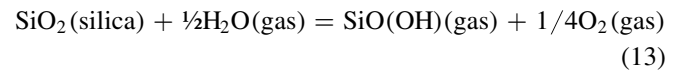
5. RESULTS FOR PURE OXIDES

5.1. Partial Pressures of $Si(OH)_4$ and Other Si–O–H Gases in Steam

We now describe our first set of calculations. As discussed earlier in Section 3, silica dissolves in steam primarily via
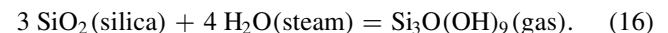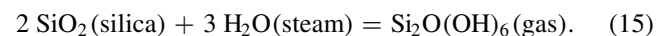
$$SiO_2(silica) + 2H_2O(steam) = Si(OH)_4(gas).$$
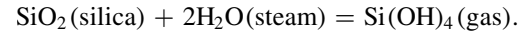
However, Hildenbrand & Lau (1994, 1998) reported SiO, SiO_2, SiO(OH), and $SiO(OH)_2$ but not $Si(OH)_4$ in a gas-leak Knudsen cell study of liquid silica reacting with water vapor near 2000 K at P_{H_2O} ~4 $\times$ 10^{-5} bars. They proposed silica dissolved in steam via the reactions

$$SiO_2(silica) + \tfrac{1}{2}H_2O(gas) = SiO(OH)(gas) + 1/4O_2(gas) \tag{13}$$

$$SiO_2(silica) + H_2O(gas) = SiO(OH)_2(gas). \tag{14}$$

Earlier, Krikorian (1970) proposed that reaction (13) was important at 1760 K and 0.5–1 bar steam pressure. This proposal was based on his estimated thermodynamic properties for SiO(OH), $SiO(OH)_2$, $Si(OH)_4$, and the work of Elliot (1952) on silica vaporization in steam gas mixtures. He also concluded that reaction (1) was important at 600–900 K and 1–100 bar steam pressure, at much higher pressures and lower temperatures than studied by Hildenbrand & Lau (1994, 1998).

Hashimoto (1992) used the transpiration method to study the reaction of silica with H_2O–O_2 gas mixtures at 1373–1773 K and ~1 bar pressure and found evidence for only reaction (1) and $Si(OH)_4$ gas. Opila et al. (1997) used a high-pressure sampling mass spectrometer to study reaction of silica with H_2O–O_2 gas mixtures at 1473–1673 K and 1 bar total pressure. They found that $Si(OH)_4$ was the major Si-bearing gas and concluded that $SiO(OH)_2$ was much less abundant under these conditions. Jacobson et al. (2005) did a transpiration study of silica reacting with H_2O–Ar gas mixtures at 1073–1728 K and 1 bar pressure. They found that $Si(OH)_4$ was the major Si-bearing gas and that $SiO(OH)_2$ was much less abundant under their experimental conditions. Jacobson et al. (2005) derived thermodynamic data for both gases.

As the pressure of steam increases, silica may also dissolve via reactions such as

$$2\,SiO_2(silica) + 3\,H_2O(steam) = Si_2O(OH)_6(gas). \tag{15}$$

$$3\,SiO_2(silica) + 4\,H_2O(steam) = Si_3O(OH)_9(gas). \tag{16}$$

The dimer $Si_2O(OH)_6$, trimer $Si_3O(OH)_9$, and higher polymers may become increasingly important at water-like densities (e.g., Krikorian 1970; Newton & Manning 2002; Zotov & Keppler 2002; Gerya et al. 2005; Tossell 2005). However, the exact P, T conditions at which the different polymers become important are not clear.

For example, Krikorian (1970) also proposed that $Si_2O(OH)_6$ is the major Si-bearing gas in steam at 600–900 K and 100–1000 bar pressure and that $Si_2O(OH)_6$ and $Si(OH)_4$ are about equally important at 1350 K in the 2–7 kbar range. This

Table 1
Estimated Partial Pressures of Si-bearing Gases

P_i (bar)	A	B	C	D
SiO	$\mathbf{8.6 \times 10^{-6}}$	1.6×10^{-13}	4.4×10^{-14}	2.9×10^{-8}
SiO_2	$\mathbf{6.9 \times 10^{-7}}$	6.4×10^{-11}	7.6×10^{-12}	6.9×10^{-7}
SiO(OH)	3.4×10^{-11}	6.7×10^{-15}	1.9×10^{-14}	1.3×10^{-8}
$SiO(OH)_2$	3.3×10^{-11}	5.9×10^{-9}	4.9×10^{-7}	1.5×10^{-3}
$Si(OH)_4$	3.9×10^{-15}	$\mathbf{4.1 \times 10^{-6}}$	$\mathbf{3.0 \times 10^{-1}}$	$\mathbf{8.25}$
$Si_2O(OH)_6$	7.5×10^{-26}	2.0×10^{-11}	5.4×10^{-4}	7.2×10^{-3}
Σall Si gases	9.3×10^{-6}	4.1×10^{-6}	3.0×10^{-1}	8.25

Notes. A: $T = 2000$ K, total P (P_T) $= 4 \times 10^{-5}$ bars, liquid silica + steam. B: $T = 1573$ K, $P_T = 1$ bar, cristobalite + 90% steam—10% O_2 gas mixture. C: $T = 1500$ K, $P_T = 270$ bars, cristobalite + steam. D: $T = 2000$ K, $P_T = 1100$ bars, liquid silica in steam (75%)–CO_2 (25%) atmosphere. Bold values represent the major gas(es) in each column.

proposal was based on his estimated thermodynamic data for SiO(OH), $SiO(OH)_2$, $Si(OH)_4$, and $Si_2O(OH)_6$.

However, Zotov & Keppler (2002) concluded that $Si_2O(OH)_6$ only became important at higher pressures than proposed by Krikorian (1970). They measured Raman spectra of dissolved silica species in saturated aqueous solutions of quartz and observed $Si_2O(OH)_6$ at pressures above 5–6 kbar. Their calculated concentrations of $Si(OH)_4$ and $Si_2O(OH)_6$ show significant amounts of $Si_2O(OH)_6$ at the high pressures they studied. For example, at 973 K and 5.6 ± 0.9 kbar pressure, ~37 mol% of total dissolved silica is present as $Si_2O(OH)_6$, increasing to ~55 mol% at 10.6 ± 2.3 kbar. These high concentrations of $Si_2O(OH)_6$ are in high-pressure steam with water-like densities of 780–940 kg m^{-3}. Water-rich fluids with densities in this range may be important at the boundary between the atmospheres and rocky interiors of planets such as Uranus and Neptune in our solar system (e.g., see the models in Fegley & Prinn 1986) and H_2O-rich exoplanets. Water-rich fluids such as H_2O–H_2 and/or H_2O–CO_2 may be relevant to Uranus- and Neptune-like exoplanets in other planetary systems. We note that the solubility of high-pressure polymorphs (e.g., coesite and stishovite) in water-rich fluids may be applicable to the atmosphere–"surface" interface inside water-rich exoplanets analogous to Neptune, but we do not consider this topic further here.

We used the experimental values for thermodynamic properties of $Si(OH)_4$ gas (Plyasunov 2011b, 2012), the partly experimental and partly estimated properties for $SiO(OH)_2$ gas (Allendorf et al. 1995; Jacobson et al. 2005), and the estimated thermodynamic properties for SiO(OH) gas (Allendorf et al. 1995) and $Si_2O(OH)_6$ gas (Krikorian 1970) to calculate the partial pressures of all four species for four sets of P, T conditions: (A) 2000 K and 4×10^{-5} bar, (B) 1673 K and 1 bar, (C) 1500 K and 270 bar, and (D) 2000 K and 1100 bar. These conditions correspond to the experiments of Hildenbrand & Lau (1994, 1998) and Opila et al. (1997), a steam atmosphere produced by vaporization of all water in Earth's oceans (e.g., Zahnle et al. 1988), and a steam atmosphere produced by complete outgassing of all H_2O and CO_2 in the BSE.

The results of our chemical equilibrium calculations are summarized in Table 1. They show that Hildenbrand & Lau (1994, 1998) are correct that $Si(OH)_4$ is unimportant and SiO(OH) and $SiO(OH)_2$ are more abundant at 2000 K and 4×10^{-5} bars. However, we compute that SiO (92%) and SiO_2
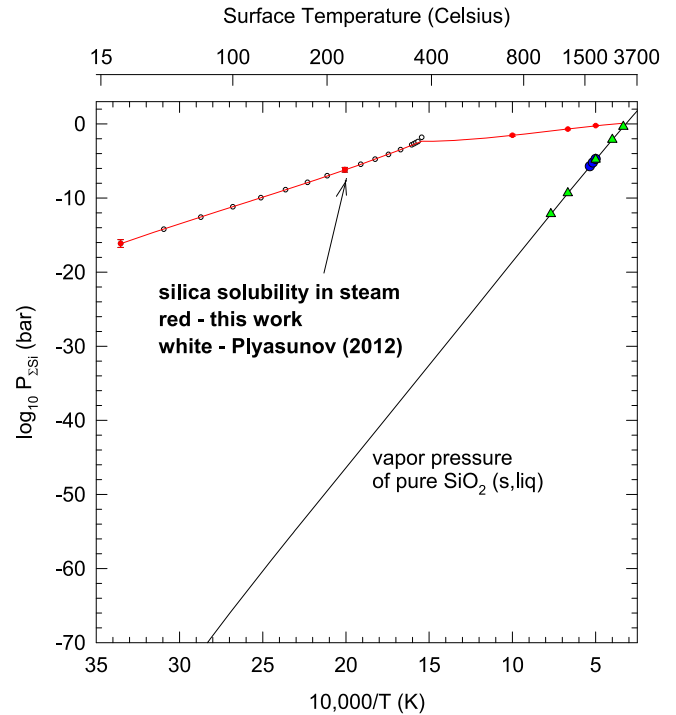

Figure 3. Enhanced volatility of silica due to its solubility in steam at P_{steam} = saturated vapor pressure of water up to 647 K, then P_{steam} = 220.64 bars—the critical pressure of water. The total amount of gaseous silicon in all forms ($P_{\Sigma Si}$) is plotted for silica in steam (red curve) and for the vapor pressure of pure silica (solid, liquid) (black curve). Silica vaporizes to a mixture of gases (SiO + O_2 + O + SiO_2 + Si) that has the same Si/O ratio as silica. Krikorian (1970) notes that the solubility of silica in steam may be limited by precipitation of hydrated silica (e.g., $SiO_2 \cdot 1/2H_2O$) below 475 K, but thermodynamic data for silica hydrates are very uncertain, and their precipitation is not shown in this graph. The total pressure ($P_{\Sigma Si}$) of Si-bearing gases in steam is dominated by $Si(OH)_4$ until very high temperatures, where SiO and SiO_2 also become important. The exact temperature depends on the total steam pressure. Representative error bars corresponding to ± 3.0 kJ mol^{-1} uncertainty in $\Delta_r G^o$ for reaction (1) (Plyasunov 2011b, 2012) are shown on the red curve. The white points are the results from Table 6 of Plyasunov (2012); the red curve represents our calculations for the same reaction using his data. Measured (Kazenas et al. 1985; blue points) and calculated (Krieger 1965; green points) vapor pressures of SiO_2 (s, liquid) agree with the calculated vapor pressure from the IVTAN code.

(8%) are the major gases under their experimental conditions. Second, we find that $Si(OH)_4$ is the major species at the other three sets of P, T conditions. For example, at 2000 K the crossover point where the abundances of SiO and $Si(OH)_4$ become equal is 0.23 bars, with $Si(OH)_4$ being the major gas at higher pressures. It remains the major gas until much higher pressures. Table 1 shows that the $Si_2O(OH)_6/Si(OH)_4$ ratio is $<9 \times 10^{-4}$ in the 1100 bar steam atmosphere. Other calculations in Section 5.2.1 show that $Si(OH)_4$ is the major species in steam at 2 kbar at temperatures $\geqslant 1300$ K, where the H_2O density is $\leqslant 322$ kg m^{-3}.

5.2. Vapor Pressure and Solubility in Steam of SiO_2, MgO, and Fe Oxides

We now describe the results of our second set of calculations. Figures 3–11 compare the total vapor pressures of the pure oxides (black curves) with solubility of the oxide in steam (red curves). The error bars on the red curves correspond to the uncertainties in the standard Gibbs energies of $Si(OH)_4$, $Mg(OH)_2$, $Fe(OH)_2$, $Ca(OH)_2$, $Al(OH)_3$, and $Ni(OH)_2$ and are
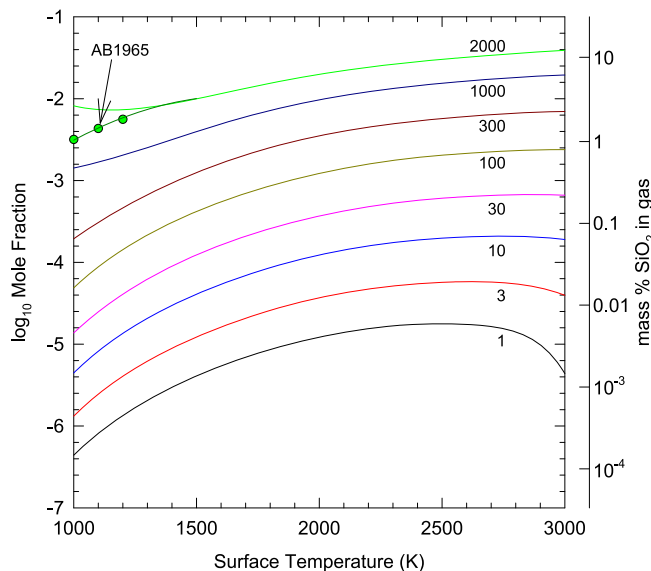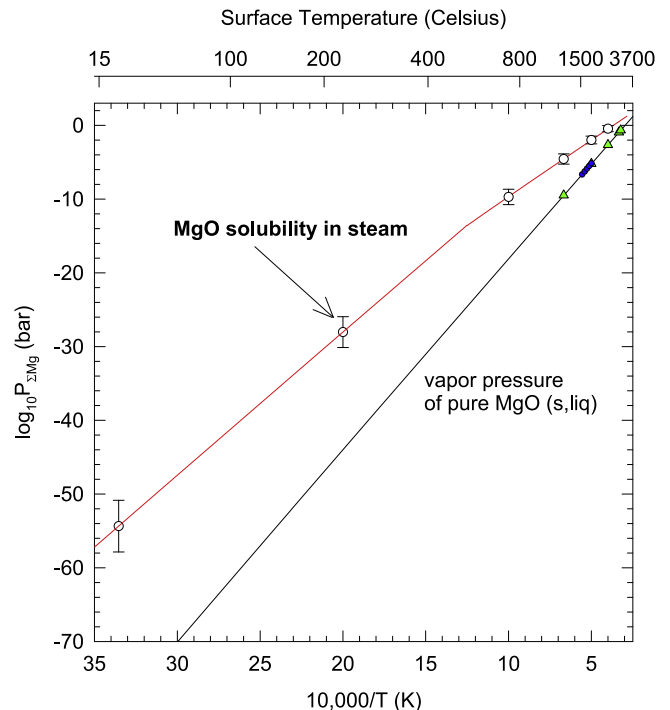
Figure 4. Silica solubility isobars in steam from 1 to 2000 bars of pressure. Solubility is expressed as mass% silica in steam and as the mole fraction of orthosilicic acid vapor $Si(OH)_4$. The 1000–1200 K points on the 2000 bar isobar are above the maximum density of 322 kg m^{-3} at which the $Si(OH)_4$ fugacity coefficients are reliable (see text and Plyasunov 2012). The three green points from Anderson & Burnham (1965) show the "true" solubility of silica at these points, and they blend smoothly into the 2000 bar isobar at 1300 K, where $\rho_{steam} \sim 322$ kg m^{-3}.

Figure 5. Enhanced volatility of MgO (periclase) in steam compared to the vapor pressure of pure MgO (solid, liquid). The total amount of gaseous magnesium in all forms ($P_{\Sigma Mg}$) is plotted for MgO dissolved in steam and for the vapor pressure of pure MgO (solid, liquid). The red curve is the total amount of Mg in all forms ($P_{\Sigma Mg} = P_{Mg(OH)2} + P_{MgOH} + P_{Mg} + P_{MgO} + P_{MgH}$) dissolved in steam. The solubility of MgO in steam is limited by precipitation of $Mg(OH)_2$ at temperatures below 780 K. Representative error bars corresponding to ± 20 kJ mol^{-1} uncertainty in $\Delta_r G^o$ for reaction (26) are shown on the red curve. The black curve is the vapor pressure ($P_{\Sigma Mg}$) of pure MgO (solid, liquid). Periclase vaporizes to a mixture of gases ($Mg + O_2 + O + O_3 + MgO + Mg_2$) that has the same Mg/O ratio as MgO. Measured (Kazenas et al. 1983; blue points) and calculated (Krieger 1966a; green points) vapor pressures of MgO (s, liquid) agree with the calculated vapor pressure from the IVTAN code.

described in the figure captions. All of these figures cover the same temperature range of 288.15–3500 K. The lower temperature of 288.15 K (15 C) is the global average surface temperature on Earth. The upper temperature of 3500 K is above the estimated surface temperatures of all known hot rocky exoplanets and above the 1 bar melting points of essentially all minerals and rocks (except ThO_2, which melts at 3640 ± 40 K; Ackermann et al. 1963). As discussed in Section 2.2, at 1 bar dry peridotite starts to melt at 1390–1473 K and is completely molten by ~1970 K.

We show oxide solubility in steam along the H_2O vapor pressure curve up to the critical point of pure water at 647.096 K (Wagner & Pruss 2002) and then at a constant steam pressure of 220.64 bars, which is the pressure at the critical point (called the critical isobar in our discussion below). The solubility of each oxide in steam is the sum of the partial pressures of all gases of the respective element (e.g., all Si-bearing gases for SiO_2, all Mg-bearing gases for MgO, and all Fe-bearing gases for Fe oxides). Likewise, the total vapor pressure of each pure oxide is the sum of the partial pressures of all gases in the saturated vapor in equilibrium with the solid or molten oxide, e.g., $Mg + O_2 + O + MgO + Mg_2$ for MgO.

The vapor pressure curves were calculated using the IVTAN code and database (Gurvich et al. 1983, 1989). We emphasize that the vapor pressure curves are calculated from the temperature-dependent standard Gibbs free energies of the solid and gases. With one exception discussed later (Fe_3O_4), the curves are not extrapolations of high-temperature vapor pressure data. We compare the IVTAN code calculations for vapor pressures of the pure oxides to representative values from other calculations and measurements where data are available. Vapor pressures were measured by Knudsen effusion mass spectrometry (KEMS; Drowart et al. 1960; Grimley et al. 1961; Chervonnyi et al. 1977; Kazenas et al. 1983, 1985; Kazenas &

Tagirov 1995; Samoilova & Kazenas 1995) and manometry (Salmon 1961). Oxygen fugacities (partial pressures) were measured using solid-state zirconia sensors (Blumenthal & Whitmore 1961; Jacobsson 1985; O'Neill 1988; O'Neill & Powneceby 1993). We refer the reader to the experimental and/ or theoretical papers cited for each oxide for details of the experimental measurements and /or calculations.

In our discussion below we use 2000 K—just above the liquidus temperature of peridotite—as a reference temperature for comparing oxide solubility in steam and the vapor pressure of the pure oxide. Our 2000 K reference temperature is well within the range of substellar equilibrium temperatures for several hot rocky exoplanets (e.g., ~1475 K for Kepler-36b, ~1570 K for Kepler-93b, 2425 K for CoRoT-7b, ~2670 K for 55 Cnc e, and ~3010 K for Kepler-10b; Kite et al. 2016).

5.2.1. Silica

Silica is the most abundant oxide in Earth's continental crust (~69 mol%) and the second most abundant oxide in the BSE (~40 mol%; see Tables 2 and 3). It also has the highest solubility in steam of rocky oxides. Figure 3 compares the vapor pressure of solid and liquid ($T \geqslant 1996$ K) SiO_2 (the black curve) with the solubility of silica in steam (the red curve). The
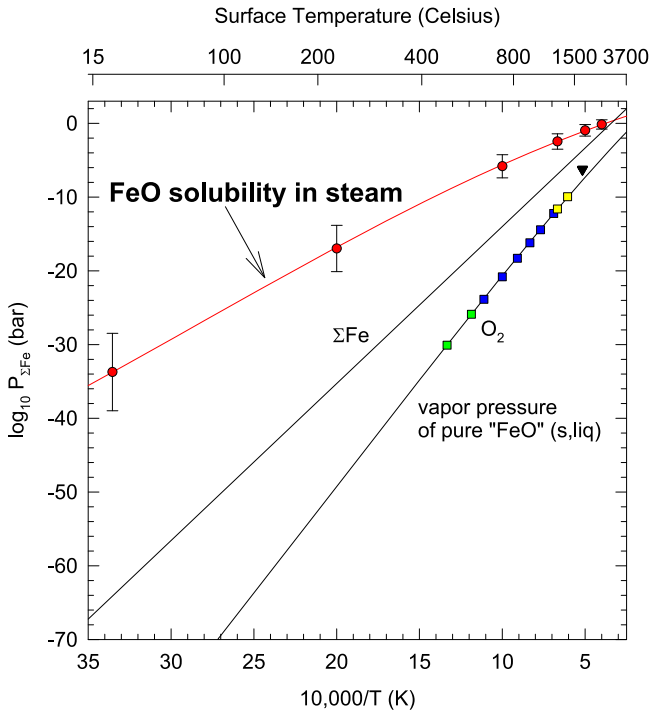
Figure 6. Enhanced volatility of "FeO" (wüstite) in steam is compared to the vapor pressure of pure "FeO" (solid, liquid). The red curve is the total amount of Fe in all forms ($P_{\Sigma Fe} = P_{Fe(OH)2} + P_{FeOH} + P_{FeO(OH)} + P_{Fe} + P_{Fe2} + P_{FeO} + P_{FeO2} + P_{FeH}$) dissolved in steam. The black curves are the partial vapor pressures of Fe gases ($P_{\Sigma Fe} \sim P_{Fe} \sim P_{vap}$) and O_2 of pure metal-saturated "FeO" (wüstite, liquid) at $T \geqslant 843$ K, the wüstite eutectoid temperature. Below 843 K the black curves are the partial vapor pressures of Fe and O_2 over metal-saturated magnetite. The blue and green squares are solid-state zirconia sensor fO_2 measurements by O'Neill (1988) for wüstite and magnetite, respectively. The yellow squares are solid-state zirconia sensor fO_2 measurements by O'Neill & Pownceby (1993) for wüstite. The black triangle is a set of fO_2 measurements for liquid FeO by Knudsen effusion mass spectrometry by Kazenas & Tagirov (1995). Representative error bars corresponding to ± 30 kJ mol^{-1} uncertainty in the data for Fe(OH)$_2$ gas (Gurvich et al. 1983) are shown on the red curve.

Figure 7. Enhanced volatility of Fe$_3$O$_4$ (magnetite) in steam compared to the vapor pressure of pure Fe$_3$O$_4$ (solid, liquid). The red curve is the total amount of Fe in all forms ($P_{\Sigma Fe} = P_{Fe(OH)2} + P_{FeOH} + P_{FeO(OH)} + P_{Fe} + P_{Fe2} + P_{FeO} + P_{FeO2} + P_{FeH}$) dissolved in steam. The black curves are the partial vapor pressures of Fe and O_2 of metal-rich Fe$_3$O$_4$ (magnetite) and liquid Fe$_3$O$_4$ ($T \geqslant 1870$ K). The pink circles (Jacobsson 1985) and green squares (O'Neill 1988) are solid-state zirconia sensor fO_2 measurements. The two blue triangles are O_2 partial pressures read off the Fe–O phase diagram of Muan & Osborn (1965). Representative error bars corresponding to ± 30 kJ mol^{-1} uncertainty in the data for Fe(OH)$_2$ gas (Gurvich et al. 1983) are shown on the red curve.
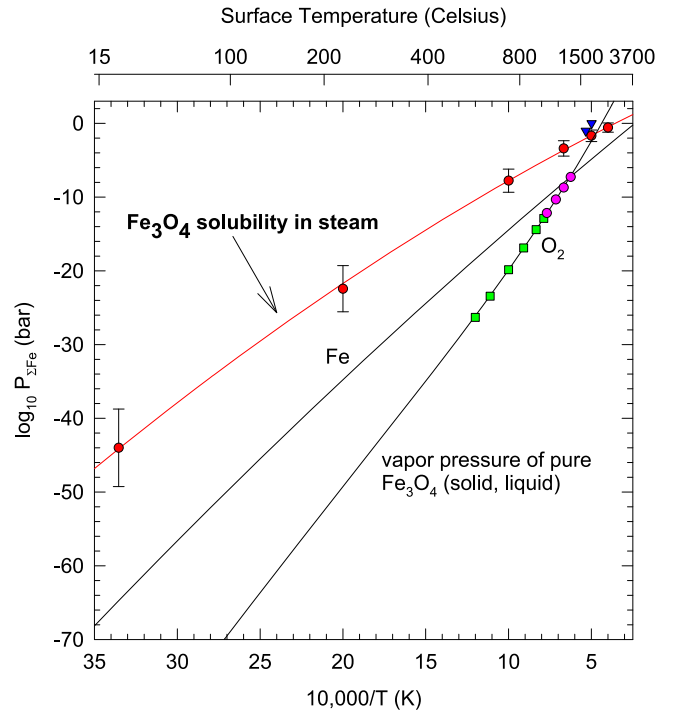
silica vapor pressure curve is simpler to explain, and we discuss it first.

Silica vaporization produces a mixture of gases with an O/Si ratio of 2, as in SiO$_2$. The vapor pressure (P_{vap}) is the sum of partial pressures of all gases in the mixture

$$P_{vap} = P_{SiO} + P_{O2} + P_O + P_{SiO_2} + P_{Si} + P_{O_3} + P_{Si_2} + P_{Si_3}.$$
(17)

At 2000 K the total vapor pressure over liquid SiO$_2$ is 1.54×10^{-5} bars and the vapor is dominantly composed of SiO (61%), O$_2$ (26%), O (8.5%) and SiO$_2$ (4.5%). Liquid silica "boils" at 3130 K, where the total vapor pressure is 1 bar and the vapor is dominantly composed of SiO (57%), O$_2$ (24%), SiO$_2$ (10%), and O (9%). All other gases (including ions) are less abundant than these four major gases. Measured (Kazenas et al. 1985, blue points) and calculated (Krieger 1965, green points) vapor pressures of SiO$_2$ (s, liquid) agree with the calculated vapor pressure (black curve) from the IVTAN code.

In contrast, the amount of silica dissolved in steam corresponds to a significantly higher pressure (at the same temperature) than the vapor pressure curve until very high temperatures (~3000 K). The total pressure ($P_{\Sigma Si}$) of silica dissolved in steam is dominated by Si(OH)$_4$ until very high temperatures where either SiO or SiO$_2$ reaches the same abundance. The exact temperature depends on the total steam pressure and is 2000 K ($P_{steam} = 0.23$ bars), 2200 K ($P_{steam} = 1$ bar), 2500 K ($P_{steam} = 10$ bars), and >3000 K ($P_{steam} = 100$ bars). At 2000 K, the total pressure of silica dissolved in steam along the critical isobar is ~0.59 bars, all of which is Si(OH)$_4$ gas. This is ~38,000 times higher than the vapor pressure of silica at the same temperature.

As discussed in Sections 3 and 5.1, dissolution of silica (SiO$_2$) in steam primarily proceeds via formation of orthosilicic acid vapor Si(OH)$_4$,

$$SiO_2 (silica) + 2H_2O(gas) = Si(OH)_4 (gas).$$
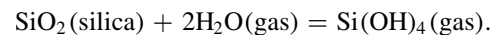
The equilibrium constant for reaction (1) is

$$K_1 = \frac{f_{Si(OH)_4}}{a_{SiO_2} f_{H_2O}^2}.$$
(18)

The fugacity (f_i) of each gas is the product of its partial pressure (P_i) and fugacity coefficient (ϕ_i). The fugacity coefficient equals unity for an ideal gas and is either >1 or <1 for a real gas. The thermodynamic activity (a_i) of silica is unity at 1 bar pressure for pure silica and is proportional to its mole fraction in silicate magma. The proportionality constant is the activity coefficient (γ_i), which is unity for an ideal solution and is either >1 or <1 for a non-ideal solution.
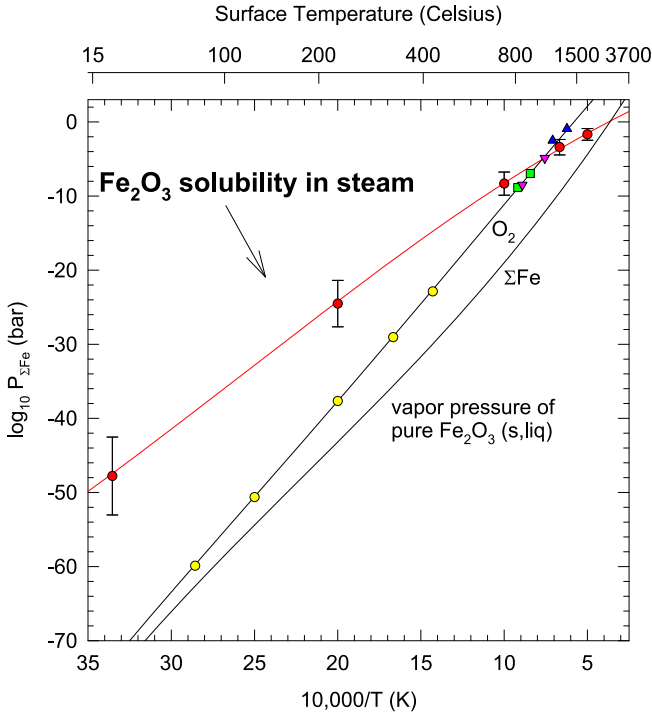
Figure 8. Enhanced volatility of Fe_2O_3 (hematite) in steam compared to the vapor pressure of pure Fe_2O_3 (hematite) and liquid Fe_2O_3 ($T \geqslant 1895$ K). The red curve is the total amount of Fe in all forms ($P_{\Sigma Fe} = P_{Fe(OH)2} + P_{FeOH} + P_{FeO(OH)} + P_{Fe} + P_{Fe2} + P_{FeO} + P_{FeO2} + P_{FeH}$) dissolved in steam. The two black curves are the vapor pressure of O_2 and of all Fe gases ($P_{\Sigma Fe}$) of pure Fe_2O_3 (solid, liquid). The yellow circles are calculated using the $\Delta G°$ equation of Hemingway ([1990]) for the fO_2 of coexisting magnetite + hematite. The blue, green, and pink points are measurements by Salmon ([1961]), Jacobsson ([1985]), and Blumenthal & Whitmore ([1961]) of the O_2 partial pressure of hematite saturated with magnetite (i.e., along the magnetite–hematite phase boundary in the Fe–O phase diagram). Representative error bars corresponding to ± 30 kJ mol^{-1} uncertainty in in the data for $Fe(OH)_2$ gas (Gurvich et al. [1983]) are shown on the red curve.

Figure 9. Enhanced volatility of CaO (lime) in steam compared to the vapor pressure of pure CaO (lime) and liquid CaO ($T \geqslant 3172$ K). The red curve is the total amount of Ca in all forms ($P_{\Sigma Ca} = P_{Ca(OH)2} + P_{CaOH} + P_{Ca} + P_{CaO} + P_{CaH} + P_{Ca2}$) dissolved in steam. The solubility of CaO in steam is limited by precipitation of $Ca(OH)_2$ at temperatures below 1550 K. Representative error bars corresponding to ± 15 kJ mol^{-1} uncertainty in the data for $Ca(OH)_2$ gas are shown on the red curve. The black curve is the vapor pressure ($P_{\Sigma Ca}$) of pure CaO (solid, liquid). Lime vaporizes to a mixture of gases (Ca + O_2 + O + O_3 + CaO + Ca_2) that has the same Ca/O ratio as lime. Our calculated vapor pressure curve agrees with experimental data (blue circles; Samoilova & Kazenas [1995]) and calculations (green triangles; Krieger [1967]).

We can rewrite the equilibrium constant expression for reaction ([1]) as

$$K_1 = \frac{\phi_{Si(OH)_4}}{\phi_{H_2O}^2} \cdot \frac{P_{Si(OH)_4}}{P_{H_2O}^2} \cdot \frac{1}{a_{SiO_2}}. \qquad (19)$$

The partial pressure of silicic acid vapor is thus

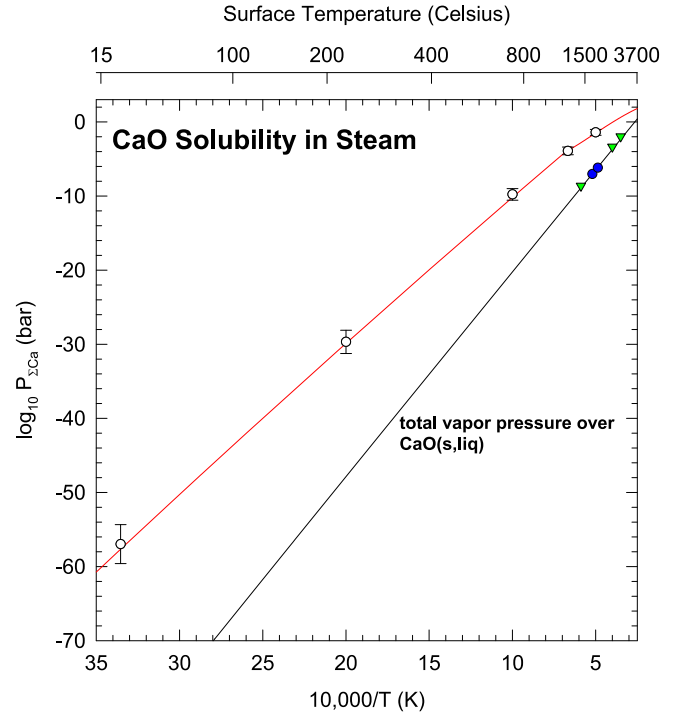$$P_{Si(OH)_4} = K_1 \cdot a_{SiO_2} \cdot P_{H_2O}^2 \cdot \frac{\phi_{H_2O}^2}{\phi_{Si(OH)_4}}. \qquad (20)$$

The equilibrium constant K_1 varies with temperature and is calculated from the standard Gibbs free energy of reaction via

$$K_1 = \exp\left(-\frac{\Delta_r G^o}{RT}\right). \qquad (21)$$

The standard Gibbs free energy of reaction $\Delta_r G^o$ is for reaction ([1]) with ideal gases at 1 bar pressure. It was calculated from thermodynamic data for $Si(OH)_4$ (g) given by Plyasunov ([2011b], [2012]) and thermodynamic data for H_2O (g) and SiO_2 (s, liq) from thermodynamic data compilations (Gurvich et al. [1983]; Chase [1998]).

The equilibrium constant expression for reaction ([1]) shows that the amount of $Si(OH)_4$, given by its mole fraction $X_{Si(OH)_4}$,

is proportional to the total pressure (P_T):

$$X_{Si(OH)_4} = P_T \cdot K_1 \cdot a_{SiO_2} \cdot X_{H_2O}^2 \cdot \frac{\phi_{H_2O}^2}{\phi_{Si(OH)_4}}. \qquad (22)$$

Thus, under otherwise constant conditions, more silica will dissolve in steam at a higher total pressure and more $Si(OH)_4$ will be produced.

Figure [4] shows the $Si(OH)_4$ mole fractions and mass% silica solubility along isobars from 1 to 2000 bars total (steam) pressure. The proportionality deduced from Equation ([22]) holds very well in the 1–2000 bar range, e.g., at 2000 K, in going from 1 to 3 to 10 to 30 to 100 to 300 to 1000 to 2000 bars the $Si(OH)_4$ mole fraction increases by factors of 3.0, 10.1, 31.7, 101, 292, 803, and 1,656 times, respectively. Deviations from the exact linear proportionality are due to small changes with temperature and pressure of the product

$$a_{SiO_2} \cdot \frac{\phi_{H_2O}^2}{\phi_{Si(OH)_4}}. \qquad (23)$$

For example, at 2000 K and 2000 bars, this product equals 0.828 (thus giving 2000 = 1656/0.828 for the increase in the $Si(OH)_4$ mole fraction from 1 to 2000 bar pressure). The expected linear proportionality is also affected by thermal
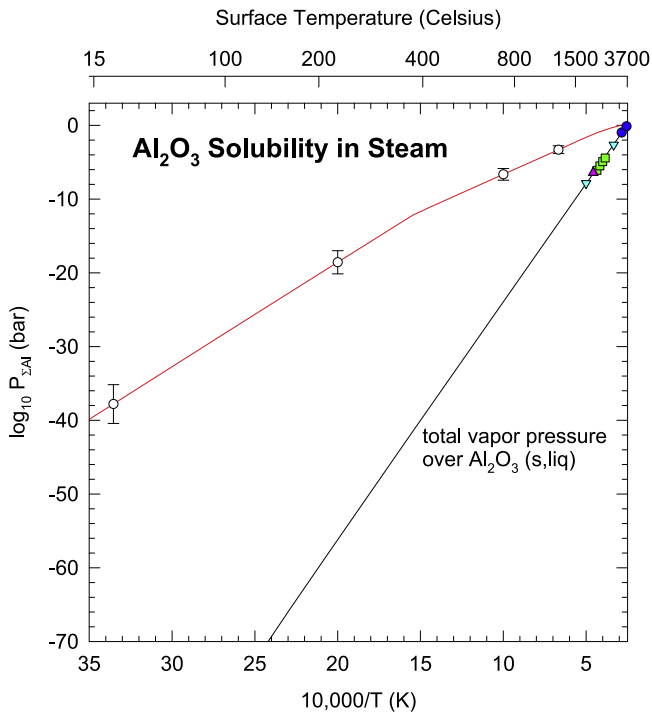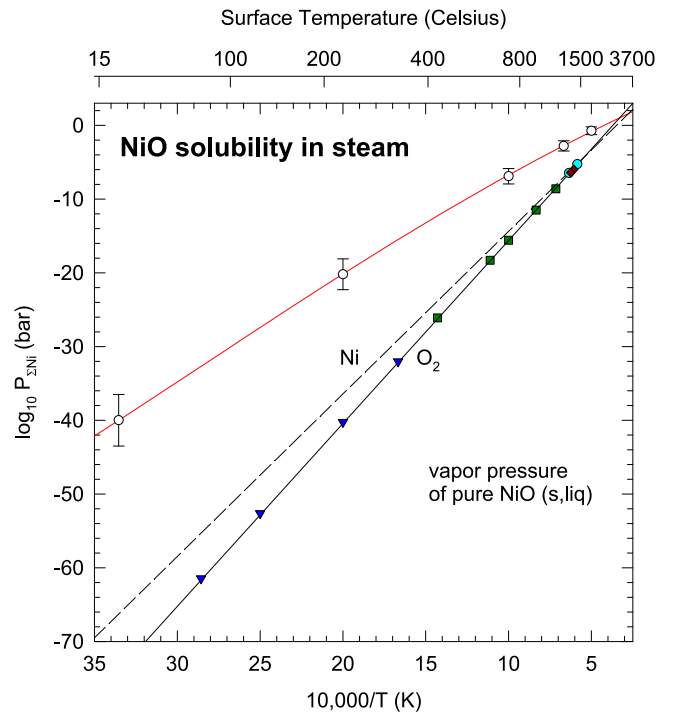
Figure 10. Enhanced volatility of Al_2O_3 (corundum) in steam compared to the vapor pressure of pure Al_2O_3 (corundum) and liquid Al_2O_3 ($T \geqslant 2327$ K). The red curve is the total amount of Al in all forms ($P_{\Sigma Al} = P_{Al(OH)3} + P_{Al(OH)2} + P_{AlOH} + P_{HAlO2} + P_{HAlO} + P_{AlH} + P_{AlH2} + P_{AlH3} + P_{Al} + P_{AlO} + P_{Al2O} + P_{Al2O2} + P_{AlO2} + P_{Al2O3} + P_{Al2}$) dissolved in steam. At $T \leqslant 642$ K the solubility of Al_2O_3 in steam and thus the $Al(OH)_3$ partial pressure is limited by precipitation of AlO(OH) (diaspore). Representative error bars corresponding to ± 15 kJ mol^{-1} uncertainty in the data for $Al(OH)_3$ gas are shown on the red curve. The black curve is the vapor pressure ($P_{\Sigma Al}$) of pure Al_2O_3 (solid, liquid). Corundum vaporizes to a mixture of gases (Al + AlO + Al_2O + Al_2O_2 + AlO_2 + Al_2O_3 + Al_2+ O + O_2 + O_3) that has the same Al/O ratio as Al_2O_3. The blue circles are laser vaporization measurements of the vapor pressure of liquid Al_2O_3 (Hastie et al. 2000), the pink triangles (Drowart et al. 1960) and green squares (Chervonnyi et al. 1977) are KEMS measurements of the vapor pressure of Al_2O_3 (corundum), and the cyan triangles are calculations by Krieger (1966a, 1966b).

Figure 11. Enhanced volatility of NiO in steam compared to the vapor pressure of NiO (bunsenite) and liquid NiO ($T \geqslant 2228$ K). The red curve is the total amount of Ni in all forms ($P_{\Sigma Ni} = P_{Ni(OH)2} + P_{NiOH} + P_{Ni} + P_{NiO} + P_{NiH} + P_{Ni2}$) dissolved in steam. Representative error bars corresponding to ± 20 kJ mol^{-1} uncertainty in the data for $Ni(OH)_2$ gas are shown on the red curve. The black curves are the partial vapor pressures of Ni and O_2 of pure metal-saturated NiO. The green squares are the solid-state fO_2 measurements of O'Neill & Pownceby (1993), and the blue triangles are calculated fO_2 values using the $\Delta G°$ equation of Hemingway (1990) for NiO formation. The cyan circles are Ni partial vapor pressures measured by KEMS by Grimley et al. (1961). The dark red diamonds are KEMS Ni partial vapor pressures of Kazenas & Tagirov (1995).

Table 2
Composition of Earth's Continental Crust[a]

Oxide	mol%
SiO_2	68.92
Al_2O_3	9.92
CaO	6.46
MgO	6.08
Na_2O	3.45
Fe_2O_3[b]	2.60
K_2O	1.84
TiO_2	0.56
MnO	0.09
P_2O_5	0.08
Total[c]	100.01

Notes.
[a] Major elements; Wedepohl (1995).
[b] 25% Fe^{3+} in the crust; most Fe in the BSE is Fe^{2+}.
[c] Also includes 0.008% Cr_2O_3 and 0.0062% NiO. Volatiles that are not included in the sum are 1.91% H_2O, 0.64% C, 0.44% CO_2, 0.028% N, 0.18% F, 0.14% S, and 0.086% Cl.

dissociation of steam to H_2 and O_2 at high temperature and low pressure, which slightly decreases the steam mole fraction.

With the exception of temperatures $\leqslant 1300$ K on the 2 kbar isobar, all calculations on the graph are at mass density $\leqslant 322$ kg m^{-3}, the density at the critical point of water. This is the density range in which Plyasunov's fugacity coefficients for $Si(OH)_4$ are valid (e.g., Table 3 and Figures 7, 9, and 14 in Plyasunov 2012). The three green points show the measured SiO_2 solubility in steam at 2 kbar pressure (Anderson & Burnham 1965) at 1000, 1100, and 1200 K, where the mass density is larger than 322 kg m^{-3}. These points smoothly blend into the 2 kbar curve at 1300 K, where the steam mass density decreases to the critical value.

Figures 3 and 4 also give the maximum amount of $Si(OH)_4$ in a steam atmosphere at a given pressure and temperature. Figure 4 also shows the mass percentage of SiO_2 in the gas as a function of pressure and temperature. The activity of pure silica is greater than that of SiO_2 dissolved in a silicate melt at the same temperature and total pressure; otherwise, pure silica would precipitate out of the melt. For example, at 2000 K the SiO_2 activity in a melt with the composition of the BSE

(Table 3, henceforth BSE magma) is

$$a_{SiO_2}(BSE) = X_{SiO_2} \gamma_{SiO_2} \sim (0.40)(0.7) \sim 0.3, \qquad (24)$$

Table 3
Composition of the Bulk Silicate Earth (BSE)[a]

Oxide	mol%
MgO	47.67
SiO_2	39.48
FeO[b]	5.90
CaO	3.40
Al_2O_3	2.30
Na_2O	0.29
NiO	0.17
TiO_2	0.14
Cr_2O_3	0.13
MnO	0.10
K_2O	0.0174
H_2O	0.31
CO_2	0.044
N	7.5×10^{-4}
F	6.9×10^{-3}
Cl	4.4×10^{-3}
S	0.0326
P_2O_5	7.3×10^{-3}
Total	100.00

Notes.
[a] Computed from data in Palme & O'Neill (2014).
[b] Most Fe in the BSE is Fe^{2+}; the crust is 25% Fe^{3+}.

and the SiO_2 activity in a melt with the composition of the continental crust (Table 2, henceforth CC magma) is

$$a_{SiO_2}(CC) = X_{SiO_2} \gamma_{SiO_2} \sim (0.69)(0.85) \sim 0.6 \qquad (25)$$

versus an activity of unity for pure silica. The activity coefficients in Equations (24) and (25) are computed with the MELTS codes discussed in Section 4. The FactSage code gives similar values for silica activities of ∼0.2 for the BSE and ∼0.55 for the CC magma at 2000 K. Thus, the $Si(OH)_4$ partial pressure over the BSE magma is ∼0.3 times that over pure silica, and the $Si(OH)_4$ partial pressure over the CC magma is ∼0.6 times that over pure silica at the same total pressure of steam.

5.2.2. Periclase (MgO)

Magnesium oxide is ∼48 mol% of the BSE but only ∼6 mol% of the continental crust. Periclase is the mineralogical name for pure MgO that occurs naturally, and we use that name for pure MgO. However, most of the MgO in the BSE and CC is a constituent of other minerals. Figure 5 compares the vapor pressure of solid and liquid ($T \geqslant 3100$ K) MgO (the black curve) and its solubility in steam (the red curve).

Vaporization of MgO produces a mixture of gases with an Mg/O ratio of unity. At 2000 K the vapor pressure is ∼5.9×10^{-6} bars and the vapor is dominantly composed of Mg (61%), O_2 (24%), O (13%), and MgO (2%). The measurements (blue points) of Kazenas et al. (1983) and the calculations (green points) of Krieger (1966a) agree with the IVTAN calculations (black curve) for the vapor pressure.

Laboratory studies show that MgO dissolution in steam proceeds primarily via formation of $Mg(OH)_2$ gas (Alexander et al. 1963; Maeda et al. 1978; Hashimoto 1992),

$$MgO(periclase) + H_2O(gas) = Mg(OH)_2(gas). \qquad (26)$$
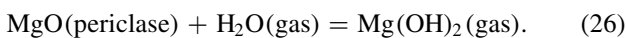
This is the reaction along the red curve at $T \geqslant 780$ K in Figure 5. However, at $T \leqslant 780$ K (the slight kink in the red curve) the solubility of MgO in steam is limited by precipitation of $Mg(OH)_2$ (brucite). This is the P, T point where the MgO (periclase)—$Mg(OH)_2$ (brucite) univariant curve intersects the solubility curve for MgO in steam. Our calculated P, T point for this intersection agrees with the measured (Kennedy 1956) position of the periclase—brucite univariant curve. Below this point the partial pressure of $Mg(OH)_2$ in steam equals the vapor pressure of brucite:

$$Mg(OH)_2(brucite) = Mg(OH)_2(gas). \qquad (27)$$

At 2000 K, the $Mg(OH)_2$ gas partial pressure in steam is ∼0.01 bars. This is ∼1750 times larger than the vapor pressure of MgO at the same temperature.

The equilibrium constant for MgO dissolution in steam via reaction (26) is

$$K_{26} = \frac{P_{Mg(OH)_2}}{P_{H_2O}} \cdot \frac{\phi_{Mg(OH)_2}}{\phi_{H_2O}} \cdot \frac{1}{a_{MgO}}. \qquad (28)$$

Rearranging Equation (28) shows that the abundance (mole fraction) of $Mg(OH)_2$ gas is independent of total pressure:

$$X_{Mg(OH)_2} = K_{26} \cdot a_{MgO} \cdot X_{H_2O} \cdot \frac{\phi_{H_2O}}{\phi_{Mg(OH)_2}}. \qquad (29)$$

Calculations from 1 to 1000 bars total pressure confirm the near constancy of the abundance of $Mg(OH)_2$ gas along an isotherm. At 2000 K, the $Mg(OH)_2$ mole fraction varies from 4.64×10^{-5} ($P_T \sim P_{steam} = 1$ bar) to 4.68×10^{-5} ($P_T \sim P_{steam} = 1000$ bars).

Figure 5 also gives the maximum amount of $Mg(OH)_2$ in a steam atmosphere at a given pressure and temperature. The activity of pure MgO is greater than that of MgO dissolved in a silicate melt at the same temperature and total pressure; otherwise, pure periclase would precipitate out of the melt. For example, at 2000 K the MgO activity in BSE magma is ∼0.2 (MELTS) to ∼0.3 (FactSage), and the MgO activity in CC magma is ∼0.01 (FactSage) to ∼0.04 (MELTS) versus an activity of unity for pure MgO.

5.2.3. Iron Oxides

Iron oxides are minor constituents of the BSE and continental crust (5.90 mol% in the BSE and 2.60 mol% in the CC). Figure 6 compares the solubility of "FeO" (denoting wüstite, which is actually $Fe_{1-x}O$ with a temperature-dependent Fe/O ratio close to 0.95) in steam (red curve) and the Σ Fe and O_2 partial vapor pressures (black curves). We first discuss the vapor pressure curves. Wüstite and the other two iron oxides vaporize incongruently (e.g., Brewer & Mastick 1951; Chizikov et al. 1971; Shchedrin et al. 1978; Kazenas & Tagirov 1995). This means that the Fe/O atomic ratio in the vapor is different from that in the solid (or liquid). The black curves are the partial vapor pressures of Fe gases ($P_{\Sigma Fe} \sim P_{Fe} \sim P_{vap}$) and O_2 over pure metal-saturated "FeO" (wüstite) at $T = 843–1650$ K and liquid "FeO" at $T \geqslant 1650$ K. The lower temperature bound is the wüstite eutectoid temperature. Wüstite is unstable at $T \leqslant 843$ K with respect to a mixture of iron metal and Fe_3O_4 (magnetite), and it decomposes to this mixture at 843 K. Below 843 K the black curves are the partial

vapor pressures of Fe and O_2 over metal-saturated magnetite. Several comparisons to experimental data are shown on the graph. The blue and green squares are solid-state zirconia sensor fO_2 measurements by O'Neill (1988) for iron—wüstite and iron—magnetite, respectively. The yellow squares are solid-state zirconia sensor (i.e., emf) fO_2 measurements by O'Neill & Pownceby (1993) for iron—wüstite. The black triangle is a set of fO_2 measurements for liquid "FeO" by KEMS by Kazenas & Tagirov (1995). As Figure 6 shows, the Fe partial vapor pressure is significantly larger than the O_2 partial vapor pressure (i.e., the oxygen fugacity, fO_2). At 2000 K the vapor pressure of liquid "FeO" is ~0.0004 bars ($P_{vap} \sim P_{Fe}$).

The red curve is the total amount of Fe in all forms ($P_{\Sigma Fe} = P_{Fe(OH)2} + P_{FeOH} + P_{FeO(OH)} + P_{Fe} + P_{Fe2} + P_{FeO} + P_{FeO2} + P_{FeH}$) dissolved in steam. $Fe(OH)_2$ is the dominant gas at all temperatures shown. Representative error bars corresponding to ± 30 kJ mol^{-1} uncertainty in the $Fe(OH)_2$ gas data (Gurvich et al. 1983) are shown on the red curve. Thermodynamic calculations predict that "FeO" dissolution in steam occurs as

$$\text{"FeO"(wüstite)} + H_2O(gas) = Fe(OH)_2(gas). \qquad (30)$$
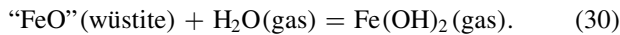
The analogous reaction involving FeO (gas) is well known (Farber et al. 1974; Rollason & Plane 2000), and Belton & Richardson (1962) showed Fe metal dissolved in steam via an analogous reaction to Equation (30). At 2000 K the $Fe(OH)_2$ gas partial pressure in steam is ~0.09 bars, which is ~220 times larger than the vapor pressure of liquid "FeO."

The equilibrium constant expression for reaction (30) is

$$K_{30} = \frac{\phi_{Fe(OH)_2}}{\phi_{H_2O}} \cdot \frac{P_{Fe(OH)_2}}{P_{H_2O}} \cdot \frac{1}{a_{FeO}}. \qquad (31)$$

The partial pressure and mole fraction of $Fe(OH)_2$ vapor are thus given by

$$P_{Fe(OH)_2} = K_{30} \cdot a_{FeO} \cdot P_{H_2O} \cdot \frac{\phi_{H_2O}}{\phi_{Fe(OH)_2}} \qquad (32)$$

$$X_{Fe(OH)_2} = K_{30} \cdot a_{FeO} \cdot X_{H_2O} \cdot \frac{\phi_{H_2O}}{\phi_{Fe(OH)_2}}. \qquad (33)$$

Equation (33) shows that the mole fraction of $Fe(OH)_2$ gas is independent of total pressure. Calculations from 1 to 1000 bars total pressure confirm the near constancy of the abundance of $Fe(OH)_2$ gas. At 2000 K, the $Fe(OH)_2$ mole fraction only varies from 4.25×10^{-4} ($P_T \sim P_{steam} = 1$ bar) to 4.27×10^{-4} ($P_T \sim P_{steam} = 1000$ bars).

Figure 7 compares the solubility of Fe_3O_4 (magnetite) in steam (red curve) and the Fe (g) and O_2 partial vapor pressures (black curves). Magnetite vaporization produces significantly more Fe gas than oxygen until high temperatures. The Fe and O_2 partial pressures are equal at ~1540 K, and O_2 is dominant at higher temperatures. The partial vapor pressure curves for Fe and O_2 are for metal-rich Fe_3O_4 and liquid Fe_3O_4 (at $T \geqslant$ 1870 K) and are computed from the partial molal Gibbs energies of oxygen and Fe metal-rich Fe_3O_4 in equilibrium with wüstite from 843 to 1573 K tabulated by Spencer & Kubaschewski (1978), i.e.,

$$RT \ln f_{O_2} = 2\Delta G_O \qquad (34)$$

$$RT \ln f_{Fe} = \Delta G_{Fe}. \qquad (35)$$

The reason for doing this is as follows. The O_2 partial vapor pressure of Fe_3O_4 coexisting with wüstite is for the reaction

$$\frac{3}{(1-4y)}Fe_{(1-y)}O + \frac{1}{2}O_2 = \frac{(1-y)}{(1-4y)}Fe_3O_4. \qquad (36)$$

The wüstite composition along the phase boundary (843–1697 K) is different from that of metal-rich wüstite and varies significantly with temperature. Neither JANAF nor IVTAN (nor any other compilation we know of) tabulates the necessary thermodynamic data to do calculations. We extrapolated the partial vapor pressure curves from 1573 K to higher temperatures. The pink circles (Jacobsson 1985) and green squares (O'Neill 1988) are solid-state zirconia sensor fO_2 measurements. These data sets are on our calculated O_2 partial vapor pressure curve. The two blue triangles are O_2 partial pressures read off the Fe–O phase diagram of Muan & Osborn (1965). They are slightly higher than our extrapolated O_2 curve. Below 843 K the curves are the same as in Figure 6 because Fe_3O_4 coexists with Fe metal in this range.

The red curve is analogous to the one in Figure 6. It shows the partial pressure of $Fe(OH)_2$ in steam due to dissolution of Fe_3O_4 via the reaction

$$Fe_3O_4(\text{magnetite}) + 3H_2O(gas)$$
$$= 3Fe(OH)_2(gas) + \frac{1}{2}O_2(gas). \qquad (37)$$
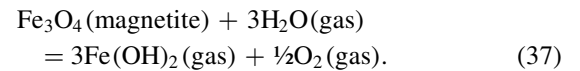
As discussed below, Belton & Richardson (1962) showed that Fe_2O_3 dissolves in steam via an analogous reaction. At 2000 K the $Fe(OH)_2$ partial pressure in steam due to dissolution of magnetite is ~0.02 bars, while the partial vapor pressure of Fe over liquid Fe_3O_4 is ~2000 times smaller and is about 10^{-5} bars.

Figure 8 compares the solubility of Fe_2O_3 (hematite) in steam with the Fe and O_2 partial vapor pressures of hematite and liquid Fe_2O_3 ($T \geqslant 1895$ K). Hematite vaporizes to almost pure O_2 with very little Fe. Figure 8 shows two vapor pressure curves for Fe_2O_3—one is the O_2 partial pressure, and the other is the sum of the pressures of all Fe-bearing gases (Fe + FeO + FeO_2 + Fe_2). The blue points (manometry; Salmon 1961), green points (emf; Jacobsson 1985), and pink points (emf; Blumenthal & Whitmore 1961) on the O_2 curve are measurements of the O_2 partial pressure by two different methods.

The red curve is analogous to the one in Figure 6. It shows the partial pressure of $Fe(OH)_2$ in steam due to dissolution of Fe_2O_3 via the reaction

$$Fe_2O_3(\text{hematite}) + 2H_2O(gas)$$
$$= 2Fe(OH)_2(gas) + \frac{1}{2}O_2(gas). \qquad (38)$$
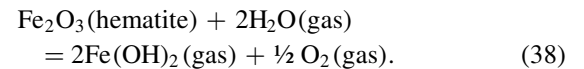
Belton & Richardson (1962) studied reaction (38) and the analogous reaction with iron metal:

$$Fe(\text{metal}) + 2H_2O(gas) = Fe(OH)_2 + H_2(gas). \qquad (39)$$
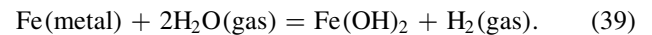
At 2000 K the $Fe(OH)_2$ partial pressure in steam due to dissolution of hematite is ~0.016 bars. The partial vapor pressure of Fe-bearing gases over liquid Fe_2O_3 is dominated by FeO_2 and is ~800 times smaller (~2×10^{-5} bars). The partial vapor pressure of Fe (g) is only 1.5×10^{-9} bars.

We focus on "FeO" dissolution in steam, reaction (30), because our MELTS and FactSage calculations show that FeO is the major Fe species in the BSE and CC magmas at the

oxygen fugacity (fO$_2$) of the steam atmospheres, e.g., at 2000 K the FeO/Fe$_2$O$_3$ activity ratio is ~155 in the BSE magma and ~20 in the CC magma.

Figure 6 also gives the maximum amount of Fe(OH)$_2$ in a steam atmosphere at a given pressure and temperature. The activity of pure "FeO" is greater than that of FeO dissolved in a silicate melt at the same temperature and total pressure; otherwise, pure wüstite would precipitate out of the melt. For example, at 2000 K the FeO activity in BSE magma is ~0.11 (FactSage) to ~0.14 (MELTS) and the FeO activity in CC magma is ~0.06 (FactSage) to ~0.15 (MELTS) versus an activity of unity for pure wüstite.

5.3. Vapor Pressure and Solubility in Steam of Less Abundant Oxides

5.3.1. Calcium Oxide

Calcium oxide (CaO, calcia, lime) is a minor constituent of Earth's continental crust (~6.5%) and BSE (~3.4%). Figure 9 compares the vapor pressure of solid and liquid ($T \geqslant 3172$ K) CaO (black curve) and its solubility in steam (red curve), which is limited by precipitation of solid and liquid Ca(OH)$_2$ at temperatures up to 1550 K.

Lime vaporizes congruently to a mixture of gases with a Ca/O ratio of unity. Our calculated vapor pressure curve agrees with measurements (blue circles; Samoilova & Kazenas 1995) and calculations (green triangles; Krieger 1967). At 2000 K the vapor pressure is ~3.6×10^{-7} bars and the vapor is dominantly composed of Ca (55%), O (35%), and O$_2$ (10%). In contrast, the total pressure of all Ca-bearing gases dissolved in steam is ~3.1×10^{-2} bars, about 84,000 times larger.

Calcium dihydroxide [Ca(OH)$_2$] is the major Ca species in steam. It forms via the reaction (Matsumoto & Sata 1981; Hashimoto 1992)

$$\text{CaO(lime, liq)} + \text{H}_2\text{O(g)} = \text{Ca(OH)}_2\text{(g)}. \qquad (40)$$
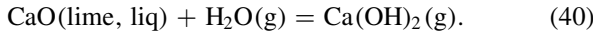
The equilibrium constant expression for this reaction is

$$K_{40} = \frac{P_{\text{Ca(OH)}_2}}{P_{\text{H}_2\text{O}}} \cdot \frac{\phi_{\text{Ca(OH)}_2}}{\phi_{\text{H}_2\text{O}}} \cdot \frac{1}{a_{\text{CaO}}}. \qquad (41)$$

Rearranging Equation (41) shows that the mole fraction of Ca(OH)$_2$ gas is independent of the total pressure,

$$X_{\text{Ca(OH)}_2} = K_{40} \cdot a_{\text{CaO}} \cdot X_{\text{H}_2\text{O}} \cdot \frac{\phi_{\text{H}_2\text{O}}}{\phi_{\text{Ca(OH)}_2}}. \qquad (42)$$

However, at $T \leqslant 1550$ K, the solubility of CaO in steam and thus the partial pressure of Ca(OH)$_2$ gas are controlled by precipitation of Ca(OH)$_2$ (portlandite). This occurs at the P, T point, where the CaO (lime)–Ca(OH)$_2$ (portlandite) univariant curve intersects the solubility curve for CaO in steam. Below this point the partial pressure of Ca(OH)$_2$ gas equals the vapor pressure of portlandite:

$$\text{Ca(OH)}_2\text{(portlandite, liquid)} = \text{Ca(OH)}_2\text{(gas)}. \qquad (43)$$
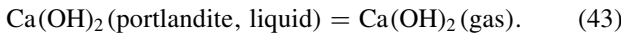
Calculations at 2000 K from 1 to 338 bars total pressure confirm the near constancy of the abundance of Ca(OH)$_2$ gas. At this temperature, the Ca(OH)$_2$ mole fraction varies from 1.39×10^{-4} ($P_T \sim P_{\text{steam}} = 1$ bar) to 1.43×10^{-4} ($P_T \sim P_{\text{steam}} = 338$ bars). Liquid Ca(OH)$_2$ forms at $P_{\text{steam}} \geqslant 338$ bars,

and the partial pressure of Ca(OH)$_2$ is controlled by the vapor pressure of liquid Ca(OH)$_2$ at $P_{\text{steam}} \geqslant 338$ bars at 2000 K.

Figure 9 also gives the maximum amount of Ca(OH)$_2$ in a steam atmosphere at a given pressure and temperature. The activity of pure CaO is greater than that of CaO dissolved in a silicate melt at the same temperature and total pressure; otherwise, pure lime would precipitate out of the melt. For example, at 2000 K the CaO activity in BSE magma is ~5.5×10^{-4} (MELTS) to ~8.3×10^{-4} (FactSage) and the CaO activity in CC magma is ~1.9×10^{-4} (FactSage) to ~6.4×10^{-4} (MELTS) versus an activity of unity for pure lime.

5.3.2. Aluminum Sesquioxide

Aluminum oxide (Al$_2$O$_3$, alumina, corundum) composes ~10% of Earth's continental crust and ~2.3% of the BSE. Figure 10 compares the vapor pressure of solid Al$_2$O$_3$ (corundum) and liquid ($T \geqslant 2327$ K) Al$_2$O$_3$ (the black curve) and its solubility in steam (the red curve). Corundum vaporizes to a mixture of gases with an Al/O ratio of 2/3. We compare the calculated vapor pressure curve to experimental data and other calculations. The blue circles are laser vaporization measurements of the vapor pressure of liquid Al$_2$O$_3$ (Hastie et al. 2000), the pink triangles (Drowart et al. 1960) and green squares (Chervonnyi et al. 1977) are KEMS measurements of the vapor pressure of Al$_2$O$_3$ (corundum), and the cyan triangles are calculations by Krieger (1966b).

At 2000 K the vapor pressure of corundum is ~1.4×10^{-8} bars and the vapor is dominantly composed of O (56.4%), Al (35.2%), AlO (6.3%), Al$_2$O (1.1%), and O$_2$ (1.0%). In contrast, the partial pressure of Al(OH)$_3$ in steam at 2000 K is ~0.02 bars, about 1,400,000 times higher.

Hashimoto (1992) and Opila & Myers (2004) showed that the dissolution of Al$_2$O$_3$ in steam proceeds via

$$\text{Al}_2\text{O}_3\text{(alumina)} + 3\text{H}_2\text{O(gas)} = 2\text{Al(OH)}_3\text{(gas)}. \qquad (44)$$
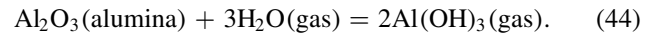
The equilibrium constant expression for reaction (44) is

$$K_{44} = \frac{P^2_{\text{Al(OH)}_3}}{P^3_{\text{H}_2\text{O}}} \cdot \frac{\phi^2_{\text{Al(OH)}_3}}{\phi^3_{\text{H}_2\text{O}}} \cdot \frac{1}{a_{\text{Al}_2\text{O}_3}}. \qquad (45)$$

Rearranging Equation (45) shows that the mole fraction of Al(OH)$_3$ gas depends on the square root of the total pressure:

$$X_{\text{Al(OH)}_3} = (K_{44} \cdot P_T \cdot a_{\text{Al}_2\text{O}_3})^{1/2} \cdot X^{3/2}_{\text{H}_2\text{O}} \cdot \left(\frac{\phi^3_{\text{Al(OH)}_3}}{\phi^2_{\text{H}_2\text{O}}} \right)^{1/2}. \qquad (46)$$

However, at $T \leqslant 642$ K, the solubility of Al$_2$O$_3$ in steam and thus the Al(OH)$_3$ partial pressure are limited by precipitation of AlO(OH) (diaspore),

$$\text{AlO(OH)(diaspore)} + \text{H}_2\text{O(gas)} = \text{Al(OH)}_3\text{(gas)}. \qquad (47)$$
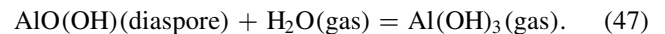
The kink in the red curve in Figure 10 is at 642 K, which is the P, T point where the diaspore—corundum univariant curve intersects the solubility curve for corundum in steam. Our calculated P, T point for this intersection is 9° higher than the measured value of 633 ± 7 K (Kennedy 1959; Fyfe & Hollander 1964; Haas 1972). This small difference is within the uncertainty of the thermodynamic data. Our calculations used $\triangle_f H^o_{298} = -1001.3 \pm 2.2$ kJ mol^{-1} and

$S_{298}^o = 35.3 \pm 0.2 \, \mathrm{J \, mol^{-1} \, K^{-1}}$ for AlO(OH) from Robie & Hemingway (1995), heat capacity measurements of Perkins et al. (1979), and $V = V(T)$ data from Pawley et al. (1996).

Figure 10 also gives the maximum amount of Al(OH)$_3$ in a steam atmosphere at a given pressure and temperature. The activity of pure Al$_2$O$_3$ is greater than that of Al$_2$O$_3$ dissolved in a silicate melt at the same temperature and total pressure; otherwise, pure corundum would precipitate out of the melt. For example, at 2000 K the Al$_2$O$_3$ activity in BSE magma is $\sim 6.3 \times 10^{-5}$ (FactSage) to $\sim 7.4 \times 10^{-3}$ (MELTS) and the Al$_2$O$_3$ activity in CC magma is ~ 0.013 (MELTS) to ~ 0.037 (FactSage) versus an activity of unity for pure corundum. The calculated Al$_2$O$_3$ activity values in silicate melt from the two codes disagree because the MELTS code does not consider solid or liquid MgAl$_2$O$_4$ (spinel), which is an important Al-bearing component in the FactSage calculations. We used the MELTS results in our calculations.

5.3.3. Nickel Oxide

Nickel oxide (NiO) is a trace constituent of the continental crust ($\sim 0.006\%$) and the BSE ($\sim 0.17\%$) and occurs as the mineral bunsenite or as a minor component of other minerals. Figure 11 compares NiO solubility in steam (red curve) with the Ni and O$_2$ partial vapor pressures of bunsenite and liquid NiO ($T \geqslant 2228$ K). The points on the vapor pressure curves are measured partial vapor pressures ($P_{\mathrm{Ni}} + P_{\mathrm{NiO}}$) (Grimley et al. 1961, cyan circles; Kazenas & Tagirov 1995, dark red diamonds), measured O$_2$ (O'Neill & Pownceby 1993, green squares), and calculated O$_2$ partial vapor pressures (Hemingway 1990, blue triangles).

At 2000 K the partial vapor pressures of Ni and NiO sum up to $\sim 3.0 \times 10^{-4}$ bars. In contrast, the total pressure of all Ni-bearing gases dissolved in steam is ~ 0.19 bars, about 630 times larger, and is 98% Ni(OH)$_2$ gas and 2% NiOH gas.

Belton & Jordan (1967) measured Ni(OH)$_2$ gas formation from Ni metal reacting with water vapor. Based on their work, Ni(OH)$_2$ gas forms via the reaction

$$\mathrm{NiO(bunsenite, \, liq)} + \mathrm{H_2O(g)} = \mathrm{Ni(OH)_2(g)}. \qquad (48)$$
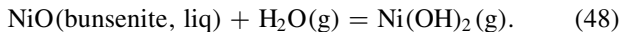
The equilibrium constant expression for reaction (48) is

$$K_{48} = \frac{P_{\mathrm{Ni(OH)_2}}}{P_{\mathrm{H_2O}}} \cdot \frac{\phi_{\mathrm{Ni(OH)_2}}}{\phi_{\mathrm{H_2O}}} \cdot \frac{1}{a_{\mathrm{NiO}}}. \qquad (49)$$

Rearranging Equation (49) shows that the mole fraction of Ni(OH)$_2$ gas is independent of the total pressure,

$$X_{\mathrm{Ni(OH)_2}} = K_{48} \cdot a_{\mathrm{NiO}} \cdot X_{\mathrm{H_2O}} \cdot \frac{\phi_{\mathrm{H_2O}}}{\phi_{\mathrm{Ni(OH)_2}}}. \qquad (50)$$

In contrast to other oxides (e.g., CaO, MgO), precipitation of Ni(OH)$_2$ does not occur at low temperatures—at least according to thermodynamic data tabulated by NIST—and the Ni(OH)$_2$ partial pressure is always limited by solubility of NiO in steam.

The red curve in Figure 11 also gives the maximum amount of Ni(OH)$_2$ in a steam atmosphere at a given pressure and temperature. The activity of pure NiO is greater than that of NiO dissolved in a silicate melt at the same temperature and total pressure; otherwise, pure NiO would precipitate out of the melt. Assuming ideality for NiO dissolved in silicate melts, lower limits to the NiO activity are given by its mole fraction in

Table 4
Hydroxide Gas Partial Pressures at 220.64 bar Steam

Gas	1000 K	1500 K	2000 K
Si(OH)$_4$	0.029	0.20	0.59
Mg(OH)$_2$	2.0×10^{-10}	2.7×10^{-5}	0.010
Fe(OH)$_2$	1.5×10^{-6}	3.5×10^{-3}	0.11
Ca(OH)$_2$	1.7×10^{-10}	1.2×10^{-4}	0.040
Al(OH)$_3$	2.3×10^{-7}	5.0×10^{-4}	0.024
Ni(OH)$_2$	1.3×10^{-7}	1.6×10^{-3}	0.19

the BSE (~ 0.002) and CC ($\sim 6 \times 10^{-5}$) magmas versus an activity of unity for pure NiO. Holzheid et al. (1997) found NiO activity coefficients $\gamma = 2.7 \pm 0.5$ in silicate melts. This would increase the NiO activity by that factor ($a_{\mathrm{NiO}} = \gamma \cdot X_{\mathrm{NiO}}$), but our conclusion remains unchanged—Figure 11 gives the maximum Ni(OH)$_2$ gas pressure.

Finally, Belton & Jordan (1967) showed that Co(OH)$_2$ also exists. However, cobalt has about $1/10$ the abundance of nickel in the BSE, and our calculations found that Co(OH)$_2$ is a very minor gas, which we do not discuss further.

5.3.4. Sodium and Potassium Oxides

Sodium oxide (Na$_2$O) and potassium oxide (K$_2$O) are too reactive to occur in nature. Thus, we did not compare their vapor pressures to their solubility in steam. We discuss the chemistry of sodium and potassium in steam atmospheres equilibrated with magma oceans in Sections 7.2–7.3.

5.4. Summary of Oxide Solubility in Steam

Table 4 summarizes our results in Figures 3–11 for the partial pressures of metal hydroxide gases in steam at 220.64 bar pressure for three selected temperatures (1000, 1500, and 2000 K). The relative solubility (or volatility) of the major rock-forming oxides in steam varies somewhat as a function of temperature, but SiO$_2$ is always the most soluble (volatile) oxide, "FeO" is the second or third most soluble (volatile), and MgO is always the least soluble (volatile).

6. SOLUBILITY OF SiO$_2$, MGO, AND FE OXIDES IN STEAM-BEARING ATMOSPHERES

Steam atmospheres are not pure water vapor, and they contain other gases due to thermal dissociation of steam (e.g., H$_2$, OH, H, O$_2$, O) and the outgassing of other volatiles from rocky material. Schaefer et al. (2012) and Fegley & Schaefer (2014) computed the major H-, C-, N-, and S-bearing gases as a function of pressure and temperature for hot rocky exoplanets with compositions like the BSE or continental crust; see Figures 7–8 of Schaefer et al. (2012) and Figure 5 in Fegley & Schaefer (2014). They found that the major gases in steam atmospheres with pressures $\geqslant 1$ bar and surface temperatures $\leqslant 2000$ K are H$_2$O, CO$_2$, N$_2$, SO$_2$, H$_2$, and O$_2$, and that CO may also be present.

Kuts (1967) studied the effects of N$_2$, CO$_2$, and O$_2$ on solubility of amorphous silica in steam at 708–913 K and 1–15 atmospheres. He found that silica solubility in the gas mixtures was the same as in pure steam at the same temperature and total steam pressure. Thus, N$_2$, CO$_2$, and O$_2$ were inert in the P, T range he studied.

We calculated the effects of a second gas on solubility of SiO$_2$, MgO, and FeO in steam as a function of composition at
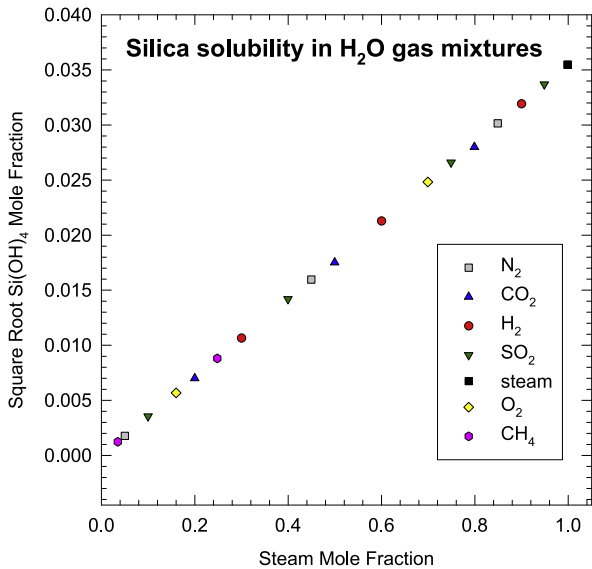
Figure 12. Calculated solubility at 300 bars and 1500 K of SiO_2 in steam and in binary gas mixtures formed by steam plus a second gas. The different points show the different gases. The square root of the $Si(OH)_4$ mole fraction is proportional to the steam mole fraction as predicted by the equilibrium constant expression (20).

Figure 13. Calculated solubility at 300 bars and 1500 K of MgO in steam and in binary gas mixtures formed by steam plus a second gas. The different points show the different gases. The $Mg(OH)_2$ mole fraction is proportional to the steam mole fraction as predicted by the equilibrium constant expression (27).

Figure 14. Calculated solubility at 300 bars and 1500 K of FeO in steam and in binary gas mixtures formed by steam plus a second gas. The different points show the different gases. The $Fe(OH)_2$ mole fraction is proportional to the steam mole fraction as predicted by the equilibrium constant expression (31).

300 bars total pressure and 1500 K. These conditions apply to a steam atmosphere formed by vaporization of an ocean of water on the early Earth (Zahnle et al. 1988). Figures 12–14 show our results for binary mixtures of steam with other abundant gases (e.g., N_2, CO_2, H_2, SO_2, O_2, and CH_4) in steam atmospheres according to published calculations (Schaefer et al. 2012; Fegley & Schaefer 2014). The different points on the graphs indicate the different binary mixtures. In the case of SiO_2 the points form a straight line given by

$$\sqrt{X_{Si(OH)_4}} \propto X_{H_2O} \tag{51}$$

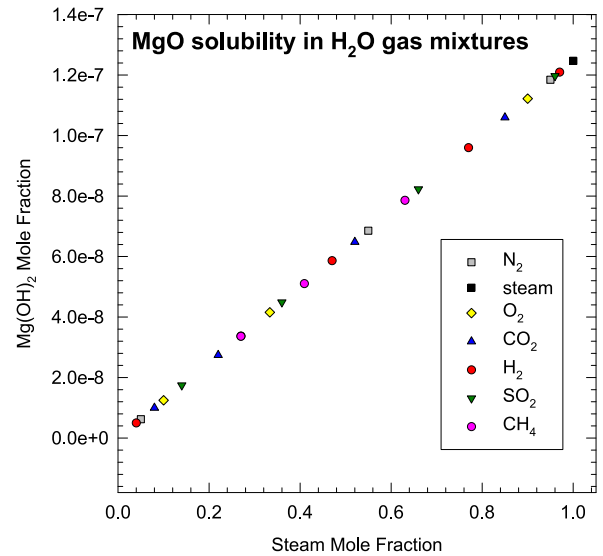as predicted from the equilibrium constant expression for Equation (1). Figures 13 and 14 show straight lines given by

$$X_{Mg(OH)_2} \propto X_{H_2O} \tag{52}$$
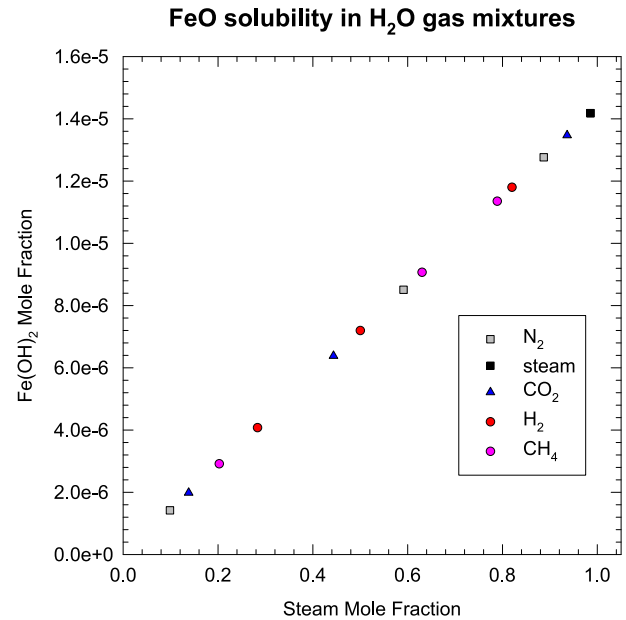
$$X_{Fe(OH)_2} \propto X_{H_2O} \tag{53}$$

as expected from the equilibrium constant expressions for Equations (26) and (30). In all three cases the second gases are inert dilutants, as expected from Kuts (1967).

7. CHEMICAL EQUILIBRIA BETWEEN STEAM ATMOSPHERES AND MAGMA OCEANS

Now we discuss our third set of calculations for the partial pressures of metal hydroxide gases formed by reactions of steam atmospheres and magma oceans having either the composition of the continental crust (CC, Table 2) or the BSE (Table 3). We first describe the temperature range over which the magma oceans exist. Next we discuss the major gases in the steam atmospheres, then all the metal hydroxide gases together, and then we consider the relative importance of hydroxide and halide gases for Si, Mg, Fe, Al, Ca, Na, and K. A series of plots are needed to display the complex chemistry in the steam atmospheres.

7.1. Solidus and Liquidus Temperatures for the BSE and CC Magmas

The solidus temperature where the first melt forms is the minimum temperature where magma can exist. A magma ocean with fluid-like behavior exists at $T \geqslant$ the lock-up temperature (T_{lock}), where the melt fraction is $\geqslant 10\%$–40% (Abe 1993). At $T_{sol} \leqslant T < T_{lock}$ the magma ocean has much higher viscosity, has solid-like behavior, and contains less water (per unit mass) than a fully molten magma ocean. The liquidus temperature is the maximum temperature where solid rocks exist. The

maximum temperature for existence of a magma ocean is the critical curve along which the liquid–vapor distinction vanishes (e.g., see the discussion in chapter 6 of Rowlinson & Swinton 1982). Estimates for the critical temperature of pure silica range from ~4700 to ~13,500 K (Table 1 in Melosh 2007), and it is plausible that the critical curves for the continental crust and BSE are within the same temperature range. These temperatures are much higher than the estimated surface temperatures of hot rocky exoplanets, and we do not consider the critical temperature of magma oceans further in this paper.

7.1.1. Continental Crust Magma Ocean

We consider a magma ocean with the composition of the average continental crust (CC, Table 2). To first approximation, the continental crust is granitic, and Goranson (1932) reported a solidus <1173 K and a liquidus of 1323 ± 50 K for Stone Mountain granite at ambient pressure (~1 bar). MELTS predicts that the continental crust solidus is 1197 K and the liquidus is 1415 K, where orthopyroxene solid solution [(Mg, Fe)$_2$Si$_2$O$_6$] is the last phase to melt. The FactSage program (with the SLAGA database) predicts a solidus of 1169 K and a liquidus of 1578 K, where hematite (Fe$_2$O$_3$) is the liquidus phase. All these values are at 1 bar pressure.

As discussed in Section 2.2, the net effect of a steam atmosphere is to lower the solidus temperature of a magma ocean because H$_2$O dissolution in the molten silicate depresses the freezing point more than the atmospheric mass increases it (via the positive Clapeyron slope). The calculated solidus temperatures (from the MELTS code) are 873 K for a 270 bar steam atmosphere and 809 K for a 1100 bar steam atmosphere (825 bars H$_2$O, 275 bars CO$_2$).

7.1.2. BSE Magma Ocean

The calculated solidus and liquidus temperatures for the BSE composition in Table 3 are 1267–1973 K (MELTS) and 1310–1938 K (FactSage with SLAGA database). Jennings & Holland (2015) used the THERMOCALC code (Powell et al. 1998) and the database of Holland & Powell (2011) and computed values of 1393–2053 K for the KLB-1 peridotite. Forsterite—rich olivine solid solution [(Mg,Fe)$_2$SiO$_4$] is the liquidus phase in all computations. For comparison, measured values for the KLB-1 peridotite are 1393–1973 K (Takahashi et al. 1993). The freezing point depressions due to H$_2$O dissolution in magma give solidus temperatures of 1206 and 1173 K, respectively, for the 270 and 1100 bar steam atmospheres.

7.1.3. Comparison of MELTS and FactSage Results for Melting Temperatures

The agreement of the calculated melting temperatures is good for the BSE composition but only satisfactory for the CC composition. However, it is about as good as the agreement of calculated values with measurements. The BSE (less so) and continental crust (more so) compositions are far removed from the optimized compositions in the FactSage databases, and the calculated melting temperatures are probably accurate to only ±(50–100) K. Thus, the solidus and liquidus temperatures from the MELTS codes are probably more realistic.

7.2. Major Gases

Figure 15 shows the abundances of major gases in steam atmospheres (with pressures of 270 and 1100 bars) in chemical equilibrium with magmas formed by the BSE and continental crust (CC). In order of decreasing abundance (mole fractions X ~ 0.8–0.01), the major gases in steam atmospheres equilibrated with CC magmas are H$_2$O > CO$_2$ > O$_2$ > HF ~ SO$_2$ > (HCl, OH, CO). The sequence in steam atmospheres equilibrated with BSE magmas is H$_2$O > CO$_2$ > SO$_2$ ~ H$_2$ > CO > (HF, H$_2$S, HCl, SO). There are a number of gases with mole fractions X ~ 0.01–0.001, including NaCl, NO, N$_2$, SO$_3$ (on the 1100 bar CC magma plot in Figure 15), S$_2$, Si(OH)$_4$, and Mg(OH)$_2$ (for the BSE plots). In general, the metal hydroxide gases have lower abundances with mole fractions X ~ 10^{-3} to 10^{-7} (see below).

7.2.1. Molecular Oxygen

Molecular oxygen is the third most abundant gas in steam atmospheres equilibrated with CC magmas, but it is not nearly as abundant (X$_{O2}$ ≪ 10^{-3}) in steam atmospheres equilibrated with BSE magmas. Earth's mantle (99.4% of the BSE by mass) is dominated by ferrous iron, with an Fe^{3+}/Σ Fe ratio of ~0.04 to ~0.11 depending on the samples analyzed and the technique used (e.g., see Canil et al. 1994; Claire et al. 2006). The lower value of ~0.04 is from Mössbauer spectroscopic analyses of relatively unaltered samples of upper mantle rocks by Canil et al. (1994). The upper value of ~0.11 is from wet chemical analyses of glasses in mid-ocean ridge basalts (MORBs) by Bézos & Humler (2005). In contrast, Earth's continental crust is richer in ferric iron, with an Fe^{3+}/Σ Fe ratio of ~0.25 (Claire et al. 2006).

The dichotomy between the oxidation states of iron in Earth's crust and mantle is due to life on Earth. Most of the oxygen produced by photoautotrophs on Earth has been consumed by geochemical reactions that produced hematite, other Fe^{3+}-bearing minerals, and sulfate minerals in Earth's continental crust, with only ~4% of all oxygen produced residing in the atmosphere today (Warneck 1989). For example, the sedimentary rocks in Earth's crust are significantly richer in ferric iron (Fe^{3+}/Σ Fe ~ 0.44) than the entire crust because of oxidation during weathering (e.g., Yaroshevsky 2006). The continental crust would be much less oxidized and hence richer in FeO-bearing minerals in the absence of life on Earth. However, abiotic production of oxygen, e.g., via solar UV photolysis of CO$_2$—as on Mars today—would still provide an oxidant for production of ferric iron in the crust of an extrasolar rocky planet.

7.2.2. Comparison to Our Prior Work

The results in Figure 15 agree with our prior work (Schaefer et al. 2012) for the major gases in steam atmospheres equilibrated with CC and BSE magmas with a few differences caused by the total pressures, volatile element abundances, and silicate magma solution models used in the calculations. The higher total pressures used in this work (270 or 1100 bars) than before (100 bars) give smaller abundances of gases produced by thermal dissociation of H$_2$O, CO$_2$, and SO$_2$, as illustrated in Figure 8 of Schaefer et al. (2012).

This work and our prior study use two different compilations for the composition of the BSE. The major element composition is very similar, but the volatile element abundances can be different. For example, Schaefer et al. (2012) used Kargel &
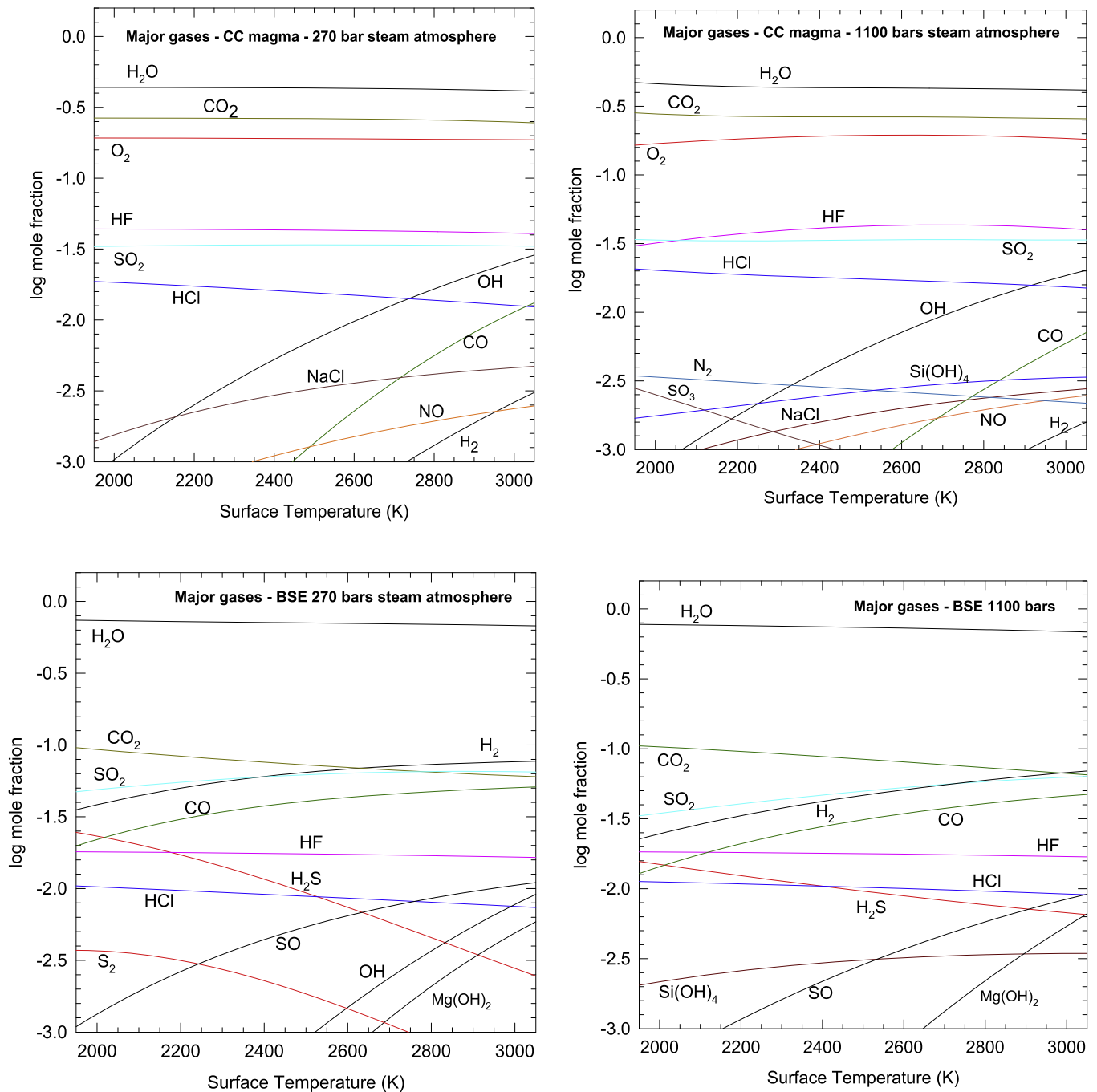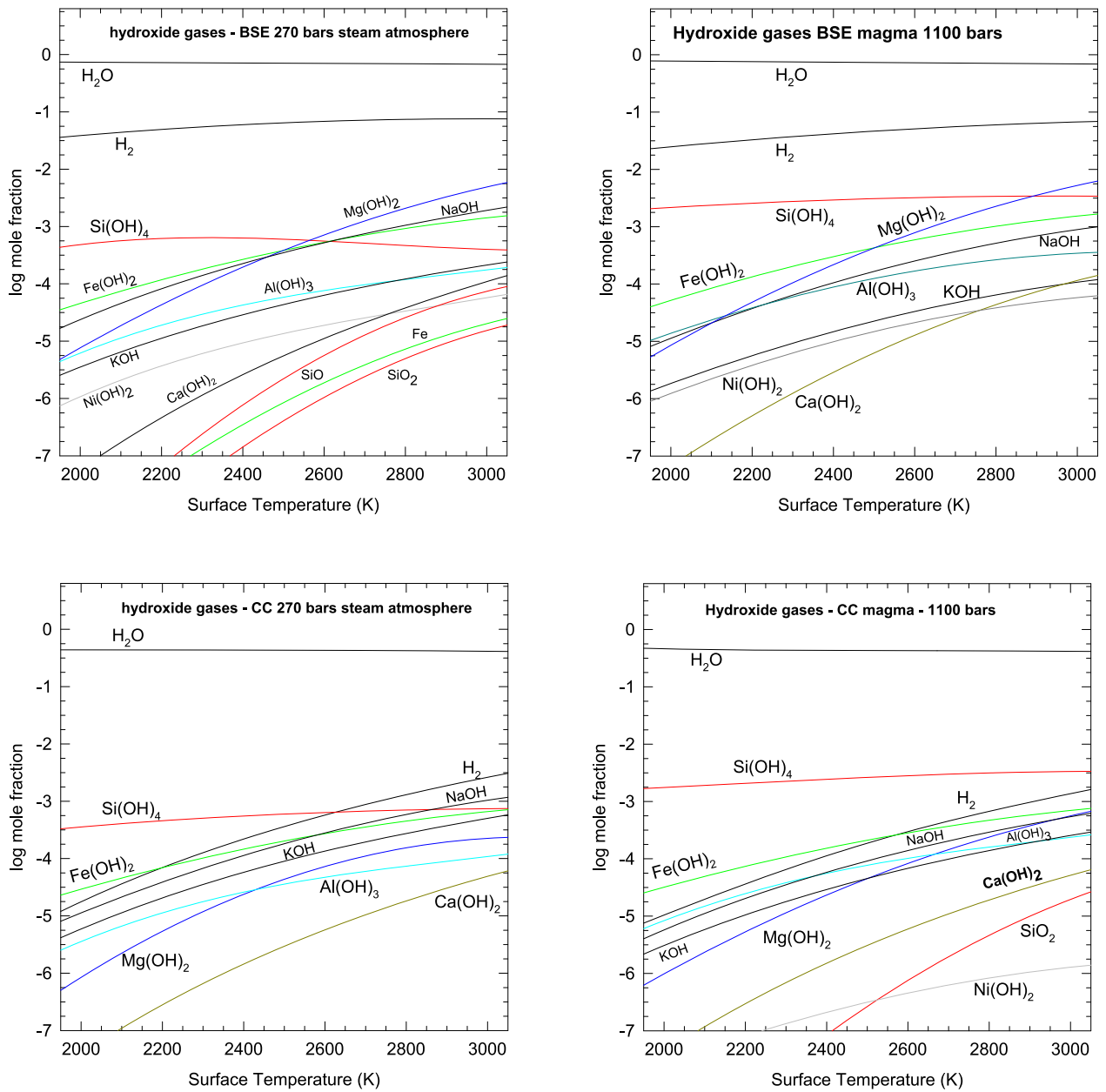
Figure 15. Abundances of the major gases in steam atmospheres (270, 1100 bars) in chemical equilibrium with bulk silicate Earth (BSE) and continental crust (CC) magmas. The same color-coding is used in all graphs.

Lewis (1993), who recommended hydrogen, carbon, and sulfur abundances of 54.7, 65, and 274 ppm, respectively, corresponding to H/C and S/C molar ratios of ∼10 and 1.6, respectively, in the BSE. In this work we use Palme & O'Neill (2014), who recommend 120 ppm H, 100 ppm C, and 200 ppm S, corresponding to H/C and S/C molar ratios of ∼14 and 0.75, respectively. This leads to H_2O/CO_2 ratios ∼40% larger and SO_2/CO_2 ratios ∼50% smaller than before in steam atmospheres equilibrated with BSE magmas (compare to Figure 2 of Schaefer et al. 2012). The abundances of N, F, and Cl are similar in the two compilations—0.88, 20.7, and 36.4 ppm, respectively, in Kargel & Lewis (1993) versus 2, 25,

and 30 ppm, respectively, in Palme & O'Neill (2014). The slightly different gas abundances in this work and our prior study are well within the range of variations shown in Figures 3–5 of Schaefer et al. (2012), which explore sensitivity of steam atmosphere chemistry to the elemental abundances used for calculations.

7.3. Metal Hydroxide and Halide Gas Chemistry

Figure 16 shows chemical equilibrium abundances of $Si(OH)_4$ and the other metal hydroxide gases in steam atmospheres of 270 and 1100 bars of pressure equilibrated with BSE or CC magma. The abundance trends for the metal
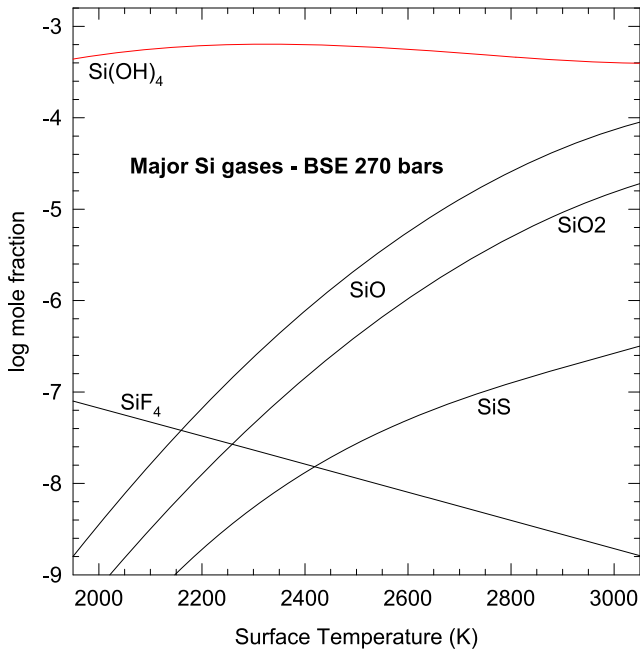
Figure 16. Chemical equilibrium abundances of the major metal hydroxide gases in 270 and 1100 bar steam atmospheres equilibrated with the BSE and CC magmas.

hydroxide gases as a function of pressure and composition are given by the equations in Sections 5.2 and 5.3 for $Si(OH)_4$ and the other hydroxide gases. For example, the $Si(OH)_4$ mole fraction at 1100 bars is $\sim5 \times$ higher than at 270 bars mainly because of the higher pressure (a factor of $\sim4.1 \times$), but also because of the slightly larger H_2O mole fraction and the slightly larger H_2O fugacity coefficient in the 1100 bar steam atmosphere. Likewise, the $Al(OH)_3$ mole fraction at 1100 bars is $\sim2 \times$ higher than at 270 bars because it is proportional to the square root of the total pressure (see Equation (46) in Section 5.3.2). However, the $Mg(OH)_2$, $Ca(OH)_2$, $Fe(OH)_2$, and $Ni(OH)_2$ abundances are nearly the same because their mole fractions are independent of the total pressure (e.g., see Equations (29), (42), and (50)) and are affected only by the smaller changes in the mole fraction and fugacity coefficient of H_2O.

Figures 17–20 show that the hydroxides are the major gases of Si, Mg, Fe, and Ni in the 270 bar steam atmosphere equilibrated with BSE magma, and this is also true for the other three cases studied (270 bar steam atmosphere equilibrated with CC magma and the 1100 bar steam atmosphere equilibrated with BSE and CC magma). However, the hydroxides are not the major Na and K gases. Figures 21 and 22 show that NaCl and KCl are the major Na and K gases, and NaF and KF are also important in the 270 bar steam atmosphere equilibrated with BSE magma. Sodium and potassium chlorides and fluorides are also important in the other three cases studied. The alkali halides are also important in the 100 bar steam atmosphere modeled by Schaefer et al. (2012)—see their Figures 1 and 2.

Figures 23 and 24 show that mixed halide—hydroxide gases (CaClOH, CaFOH and $FAl(OH)_2$, F_2AlOH, $ClAl(OH)_2$) are

Figure 17. Abundances of the major Si-bearing gases in a 270 bar steam atmosphere in chemical equilibrium with BSE magma.

Figure 18. Abundances of the major Mg-bearing gases in a 270 bar steam atmosphere in chemical equilibrium with BSE magma.

important for Ca and Al in the 270 bar steam atmosphere equilibrated with BSE magma. The mixed halide—hydroxide gases are the major species for Ca (see Figure 24), while they are about as important as $Al(OH)_3$ for Al in Figure 23. Again, similar results were obtained for the other cases not shown (270 bar steam atmosphere with CC magma and 1100 bar steam atmospheres with BSE or CC magma). Finally, under some conditions (e.g., T < 2200 K in the 1100 bar steam atmosphere equilibrated with CC magma) $FeCl_2$ may be more abundant than $Fe(OH)_2$ gas.

Hydrogen chloride and HF are the major halogen-bearing gases in the steam atmospheres considered here and by Schaefer et al. (2012). This is consistent with HCl and HF being the major Cl- and F-bearing gases in terrestrial volcanic gases, which are generally dominated by steam (Symonds et al. 1994).

The relative abundance of hydroxide and halide gases in H_2O-rich systems with HCl and HF are controlled by exchange equilibria (pp. 68–73 in Hastie 1975), e.g.,
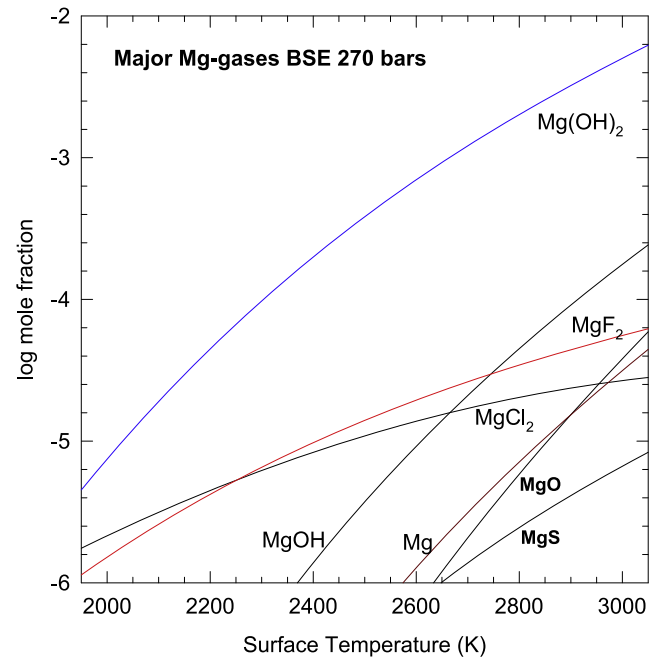
$$HCl(g) + NaOH(g) = NaCl(g) + H_2O(g). \quad (54)$$

The equilibrium constant expression for reaction (54) and analogous exchange equilibria involving other halides (e.g., NaF, KCl, KF, CaClOH, CaFOH, $FAl(OH)_2$) are independent of total pressure, e.g.,

$$K_{54} = \frac{P_{H_2O}P_{NaCl}}{P_{HCl}P_{NaOH}} = \frac{X_{H_2O}X_{NaCl}}{X_{HCl}X_{NaOH}}. \quad (55)$$
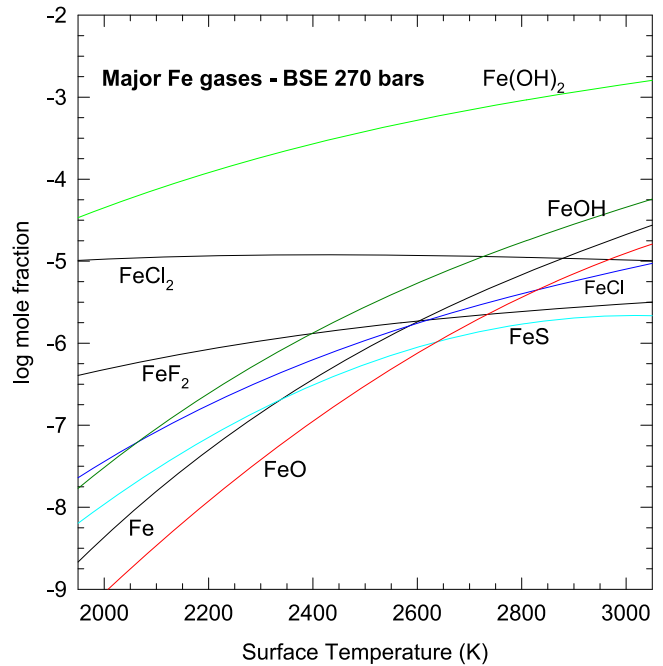
Rearranging Equation (55) shows that the molar ratio of NaOH to NaCl is proportional to the molar ratio of H_2O to HCl in the gas,

$$\frac{X_{NaOH}}{X_{NaCl}} = \frac{X_{H_2O}}{X_{HCl}} \cdot \frac{1}{K_{54}}. \quad (56)$$

At 2000 K, the equilibrium constant $K_{54} = 3365$, the H_2O/HCl ratio is ~72 (Figure 15), and the NaOH (g)/NaCl (g) molar

Figure 19. Abundances of the major Fe-bearing gases in a 270 bar steam atmosphere in chemical equilibrium with BSE magma. The curves for FeCl and FeF plot on top of each other, and only that for FeCl is shown on the graph.

ratio is ~0.02 in the 270 bar steam atmosphere equilibrated with BSE magma. A much larger H_2O/HCl ratio ≥3365, the value of the equilibrium constant for reaction (54), is needed for NaOH/NaCl ~ 1. Similarly, Hastie (1975) found that H_2O/HCl ratios of ~$10^3 - 10^4$ are needed for equal abundances of metal hydroxide and halide gases and showed that this is due primarily to differences in the M–OH and M–Cl or M–F bond dissociation energies, whereas the entropy changes for the
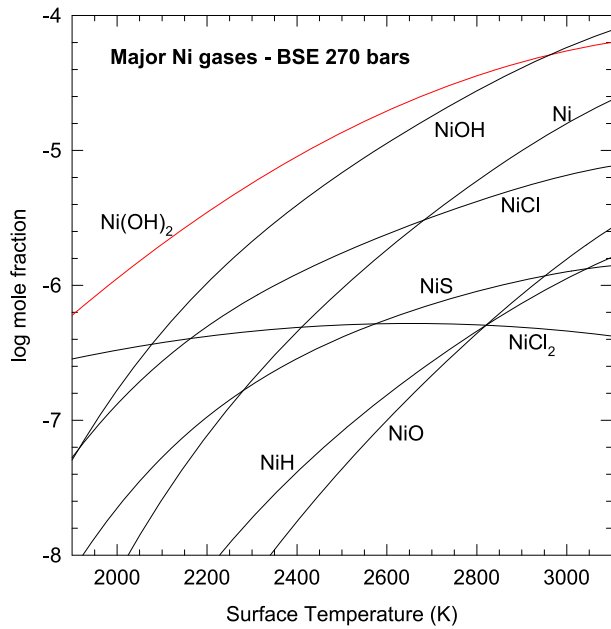
Figure 20. Abundances of the major Ni-bearing gases in a 270 bar steam atmosphere in chemical equilibrium with BSE magma.

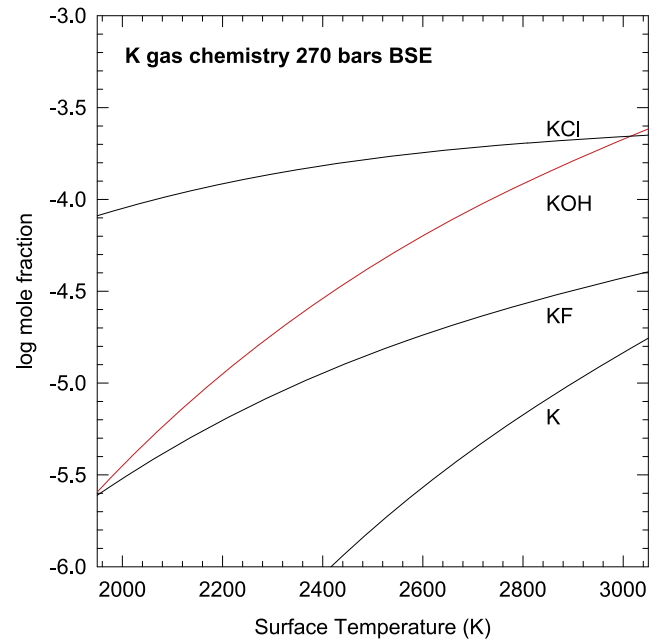**Figure 22.** Chemical equilibrium abundances of the major K-bearing gases in a 270 bar steam atmosphere in equilibrium with the BSE magma.
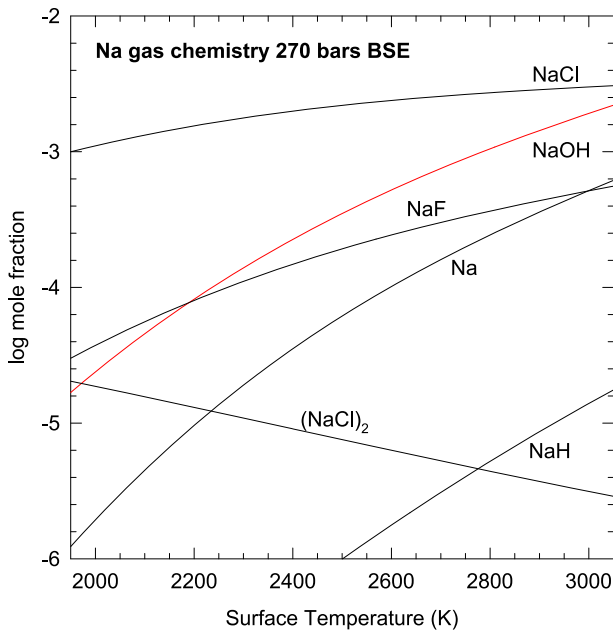
Figure 21. Chemical equilibrium abundances of the major Na-bearing gases in a 270 bar steam atmosphere in equilibrium with the BSE magma.

Figure 23. Chemical equilibrium abundances of the major Al-bearing gases in a 270 bar steam atmosphere in equilibrium with the BSE magma.

exchange reactions between hydroxides and chlorides or between hydroxide and fluorides are fairly constant for many systems.

7.4. Rocky Element Distribution between Magmas and Steam Atmospheres

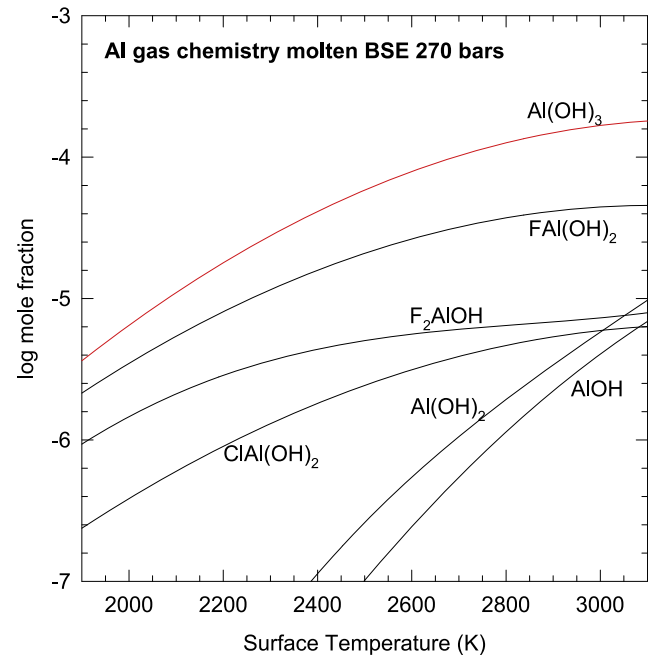In Section 5 we demonstrated the high solubility of rocky elements in pure steam, and our calculations in Section 7.2 showed the equilibrium abundances of these elements in steam atmospheres as a function of temperature, pressure, and magma ocean composition. Figures 16 and 25 illustrate the important point that fractional vaporization of rocky elements from magma oceans equilibrated with steam atmospheres changes the elemental compositions of gas and magma from the original bulk composition. Our chemical equilibrium calculations show that essentially *all* rocky element ratios in the steam atmospheres are fractionated from those in the parental magmas (except at the intersection points with the original BSE or CC composition in Figures 26–28, and their analogs for other rocky element pairs). For example, consider Si, Mg, and Fe in
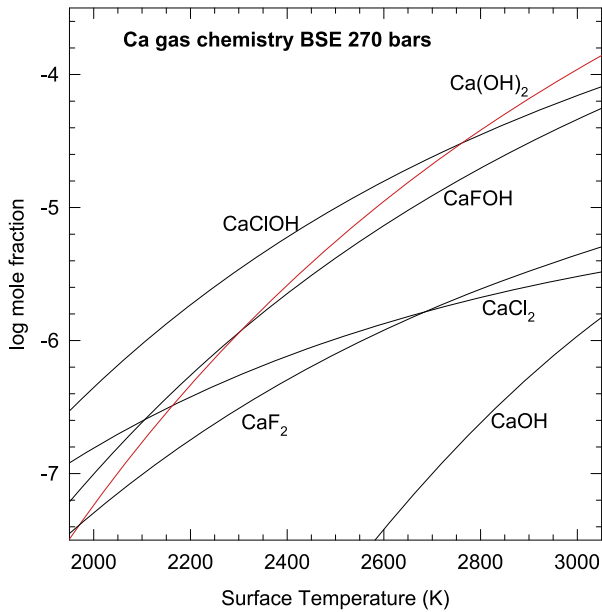
Figure 24. Chemical equilibrium abundances of the major Ca-bearing gases in a 270 bar steam atmosphere in equilibrium with the BSE magma.

the BSE. Table 3 shows that MgO, SiO$_2$, and FeO compose >90% of the BSE. Figures 26 and 27 show the molar Si/Mg and Si/Fe ratios in steam atmospheres equilibrated with magma initially having BSE composition (shown as the horizontal line). The Si/Mg ratio in the gas varies by almost a factor of 10,000 and the Si/Fe ratio by nearly a factor of 30 from 2000 to 3000 K.

At surface temperatures ~2000 K, the Si/Mg and Si/Fe ratios in the gas are higher than the original source composition, whereas at 3000 K the ratios are lower than the original ones for both total pressures (see Figures 26 and 27). This happens because more Si partitions into the steam atmospheres at temperatures around 2000 K than either Fe or Mg. Partitioning of Fe and Mg becomes much more favorable at higher temperatures. Figures 25(a) and (b) illustrate this point and also show that partitioning of Si and Fe is fairly similar at lower temperatures, so the Si/Fe ratio in steam atmospheres equilibrated with BSE magmas is less fractionated than the Si/Mg ratios in the gas.

Figure 28 is another example; it shows fractional vaporization of Si and Ca from the continental crust (SiO$_2$ + CaO > 78% of the crust; Table 2). Depending on the P, T conditions, Figure 28 shows that the Si/Ca ratio varies by nearly a factor of 100 from the initial composition (shown by the horizontal line). The Si/Ca ratio in the steam atmospheres goes from much larger (at ~2000 K) to much smaller (at ~3000 K) than the initial ratio because significantly more Ca partitions into the gas as temperature increases. Figures 25–28 demonstrate that in principle significant changes in planetary (or crustal) bulk composition, density, and internal structure are possible if atmospheric loss occurs from hot rocky planets with steam atmospheres.

We now examine the distribution (or partitioning) of rocky elements between steam atmospheres and magma oceans on hot rocky exoplanets in more detail and explore the relative importance of halide and hydroxide gases for this partitioning.

The molar distribution coefficient D in Figure 25 is defined as

$$D = \frac{N_g^E}{N_m^E}. \tag{57}$$

The moles of an element "E" in the gas (N_g^E) is the total mole fraction of an element in the gas times the total moles of gas, e.g., for sodium

$$N_g^{\mathrm{Na}} = (X_{\mathrm{Na}} + X_{\mathrm{NaF}} + X_{\mathrm{NaCl}} + X_{\mathrm{NaOH}} + X_{\mathrm{NaH}}$$
$$+ 2X_{(\mathrm{NaCl})_2} + \cdots)N_{\mathrm{gas}}. \tag{58}$$

The number of moles of element "E" remaining in the magma (N_m^E) is the total number of moles in the system (N_T^E, i.e., the total number of moles of element "E" input into the calculation) minus the amount in the gas, e.g.,

$$N_m^{\mathrm{Na}} = N_T^{\mathrm{Na}} - N_g^{\mathrm{Na}}. \tag{59}$$

The total number of moles of an element "E" is given in Table 2 for the continental crust and in Table 3 for the BSE. Note that the values for Na$_2$O (and also for K$_2$O, Al$_2$O$_3$, and Fe$_2$O$_3$) in Tables 2 and 3 have to be multiplied by two because Equations (57)–(59) are counting moles of atoms for each element.

Figures 25(b) and (d) show the molar distribution coefficients (D values) for the 1100 bar steam atmospheres equilibrated with the BSE and CC magmas, and Figure 25(c) shows the D values for the 270 bar steam atmosphere equilibrated with CC magma. All of these D values are computed with F and Cl included in the calculations (our nominal models). Figure 25(a) is slightly different because it shows two sets of D values for the 270 bar steam atmosphere equilibrated with BSE magma: either with (solid curves) or without (dashed curves) any chlorine or fluorine.

The solubility of Cl- and F-bearing gases (e.g., HCl, HF, NaCl, NaF, KCl, KF, etc.) in high-temperature silicate magmas is poorly known, and the calculations without chlorine or fluorine in the system (i.e., zero moles of Cl and F input into the calculations) simulate complete solubility of the halogens in the magma ocean. (We do not say that complete solubility of F and Cl in the magma ocean is reasonable, but it is one endmember case, with the other being all Cl and F in the steam atmosphere as in our nominal models.)

The largest effects in Figure 25(a) are observed for K, Na, Ca, and Al in roughly this order because of the importance of KCl, NaCl, CaClOH, and AlF(OH)$_2$ gases. The actual distribution coefficients for these elements will lie between the extremes indicated by the solid line (all F and Cl in the gas) and dashed line (all F and Cl in the magma). The solid and dashed lines are much closer for the other rocky elements (Ni, Mg, and Fe ~ Si) because the hydroxides are their major gases. Table 5 lists the D values for the four plots in Figure 25.

We now show how the molar distribution coefficients (D values) in Table 5 are related to partition coefficients (k_D) written in terms of concentrations. The k_D values are very useful for geochemical modeling and allow us to easily compute how much rocky element concentrations and ratios in the residual planet(s) vary from those in the original planet(s) as a function of the amount of atmosphere lost.

Rearranging Equation (59) gives the total number of moles (N_T^E) of any element "E" in the steam atmosphere—magma
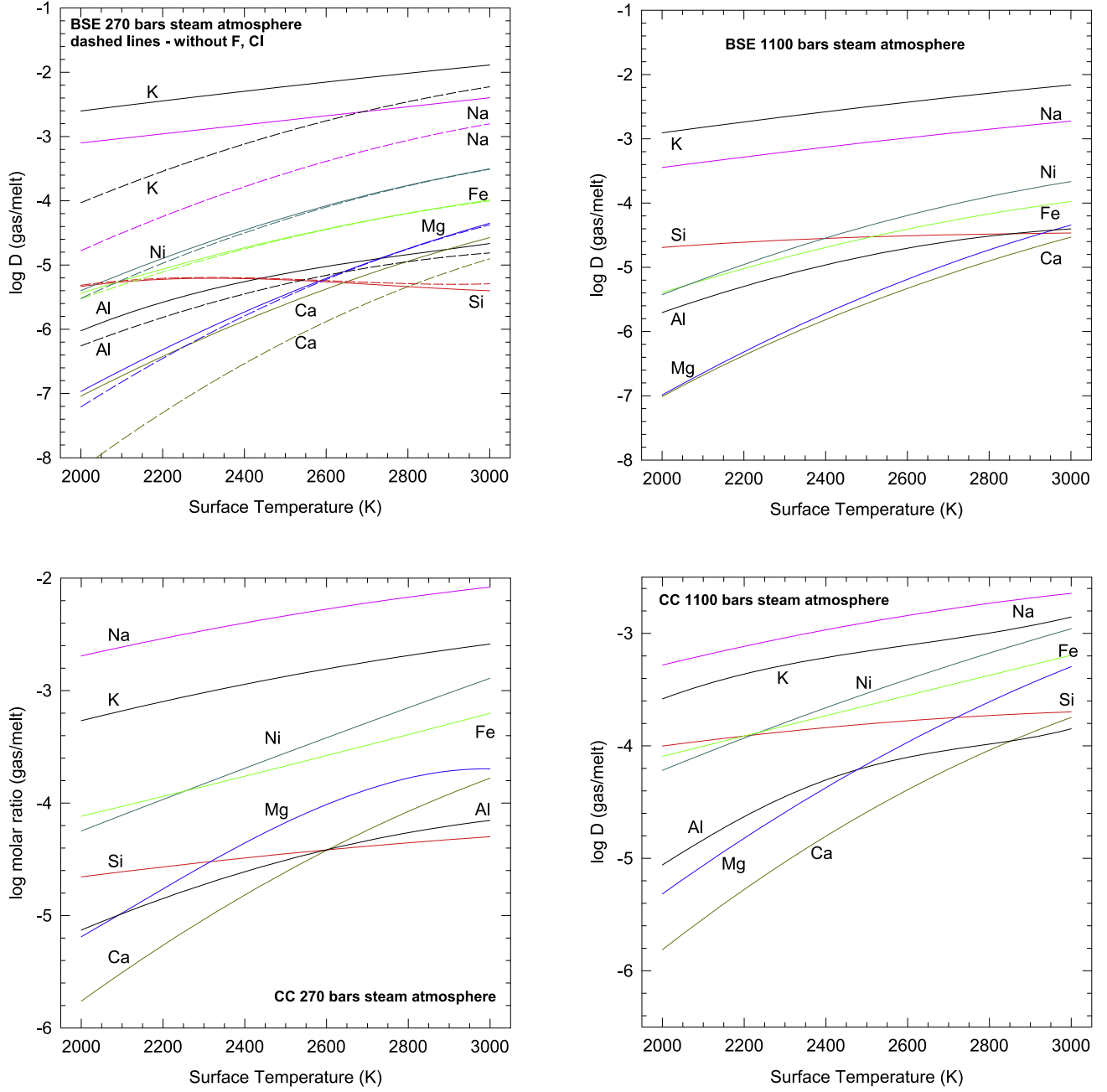
Figure 25. Gas/magma molar distribution coefficients (D) for rocky elements in the 270 or 1100 bar steam atmospheres equilibrated with BSE magma (a, b) and CC magma (c, d). The dashed curves in panel (a) are calculations without any halide gases, i.e., all F and Cl dissolved in the BSE magma ocean. The D values are defined in Equation (57) in the text.

ocean system:

$$N_T^E = N_m^E + N_g^E. \tag{60}$$

We rewrite Equation (60) in terms of concentrations (C) and mass fractions (F)

$$N_T^E = C_m^E F_m + C_g^E F_g = C_m^E F_m + C_g^E (1 - F_M). \tag{61}$$

Mass balance requires that the mass fractions sum to unity, which allows the substitution of $(1 - F_M)$ for F_g made above. We now combine Equations (57) and (61) to obtain two very

useful relationships:

$$D \equiv \frac{N_g^E}{N_m^E} = \frac{C_g^E}{C_m^E}\left(\frac{1 - F_m}{F_m}\right) = k_D\left(\frac{1 - F_m}{F_m}\right) \tag{62}$$

$$k_D \equiv \frac{C_g^E}{C_m^E} = D\left(\frac{1 - F_m}{F_m}\right)^{-1}. \tag{63}$$

The IVTAN code results show that the mass fractions of magma are fairly constant from 2000 to 3000 K and have values of 0.998 for the BSE and 0.982 for the continental crust. The k_D in Equations (62) and (63) is the partition coefficient in terms of molar concentrations. We use the Si/Mg ratio in the
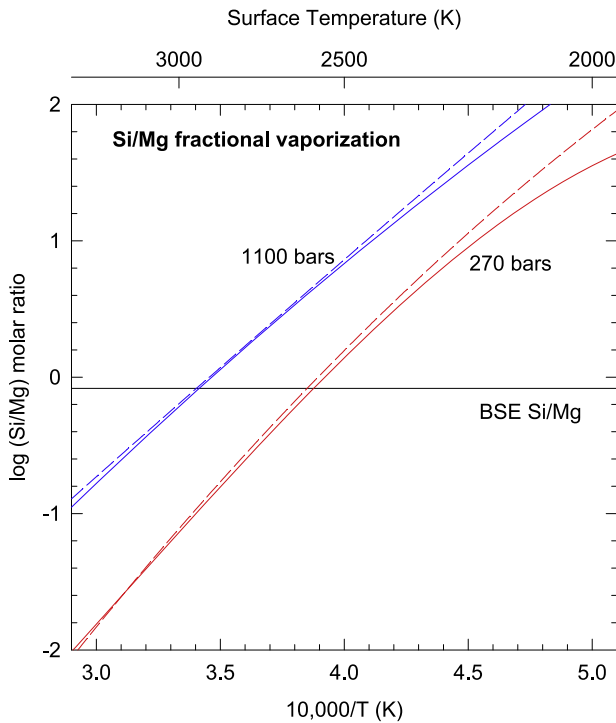
Figure 26. Fractional vaporization of Si and Mg from BSE magma into steam atmospheres with pressures of 270 bars (red) or 1100 bars (blue). The solid and dashed lines are calculations with and without halide gases, respectively. The molar Si/Mg ratios in the molten BSE magma and in the steam atmosphere are shown. The atmospheric Si/Mg ratio is greater than that in the BSE above the horizontal line and less than that in the BSE below 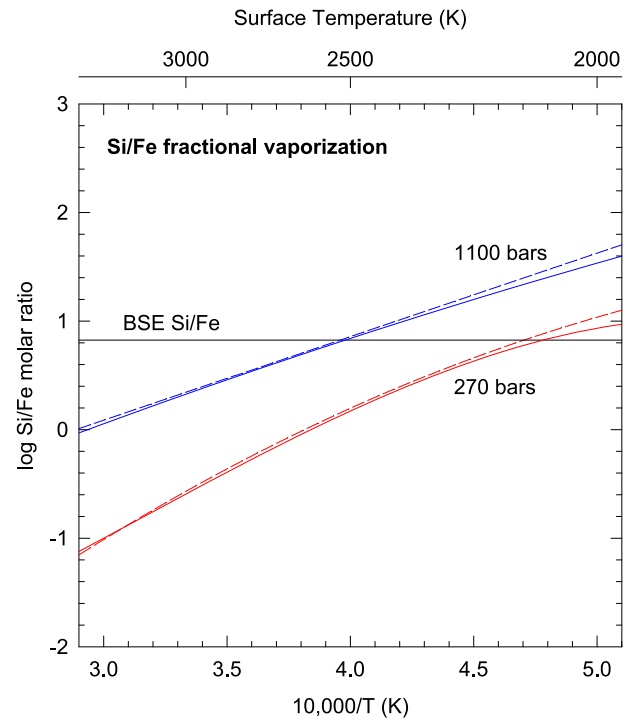the horizontal line. Thus, atmospheric loss will either deplete (cooler surface temperature) or enrich (hotter surface temperature) the residual rocky planet in Si relative to Mg. The crossover temperature depends on pressure of the steam atmosphere.

Figure 27. Fractional vaporization of Si and Fe in 270 and 1100 bar steam atmospheres in equilibrium with the BSE composition of Palme & O'Neill (2014). The atomic Si/Fe ratios in the molten BSE magma and in the steam atmosphere are shown. The atmospheric Si/Fe ratio is greater than that in the BSE above the horizontal line and less than that in the BSE below the horizontal line. Thus, atmospheric loss will either deplete (cooler surface temperature) or enrich (hotter surface temperature) the residual rocky planet in Si relative to Fe. The crossover temperature depends on pressure of the steam atmosphere.

BSE to illustrate geochemical modeling, with the partition coefficients defined in Equation (63).

7.5. Origin of the Si/Mg Ratio in the BSE

The Si/Mg molar ratio in the BSE is fairly well constrained —the mean value ($\pm 1\,\sigma$) from eight well-known geochemical tabulations is $\sim 0.82 \pm 0.03$, and a recent recommended value is ~ 0.83 (Palme & O'Neill 2014). The Si/Mg ratio in the BSE has aroused considerable interest over time because it is about 15% smaller than the solar Si/Mg ratio of ~ 0.97 (Lodders 2003) and because Si and Mg are the two most abundant rocky elements combined with oxygen in Earth. The difference between the BSE and solar composition ratios may reflect different Si/Mg ratios in Earth's upper and lower mantle (unlikely), incorporation of Si into Earth's core (plausible), and/or fractional vaporization and loss of Si and Mg during accretion of Earth (e.g., discussion in Palme & O'Neill 2014). Based on the results in Figures 26–28 and as an illustrative example, we explicitly assume that the subsolar Si/Mg ratio of the BSE is due solely to fractional vaporization into and subsequent loss of a steam atmosphere on the early Earth.

We need to use solar-normalized element ratios in our calculations. We refer to these normalized ratios as CI-normalized ratios because the solar elemental abundances of rocky elements are best determined by chemical analyses of CI chondrites (e.g., see Lodders 2003). Using Equation (63), the solar (CI chondrite)—normalized Si/Mg concentration ratio of

$0.853 (= 0.828/0.971)$ in the BSE is given by

$$\left(\frac{C^{\mathrm{Si}}}{C^{\mathrm{Mg}}}\right)_{\mathrm{BSE/CI}} \equiv \left(\frac{\mathrm{Si}}{\mathrm{Mg}}\right)_{\mathrm{BSE/CI}} = \frac{k_D^{\mathrm{Si}} + F_{\mathrm{BSE}}\left(1 - k_D^{\mathrm{Si}}\right)}{k_D^{\mathrm{Mg}} + F_{\mathrm{BSE}}\left(1 - k_D^{\mathrm{Mg}}\right)}.$$

(64)

The F_{BSE} in Equation (64) is the mass fraction of the BSE, and F_g is the mass fraction of the steam atmosphere. These two mass fractions sum to unity. The reader may ask, what about the core? The BSE and the steam atmosphere are all we need to consider for any lithophile (rock-loving) element ratio where neither element goes into the metallic core to any appreciable extent. (For a contrary view see O'Rourke & Stevenson [2016], who speculate that 1–2 mass% Mg may dissolve into Earth's core.) Here we focus on Si/Mg, but we also consider Si/Al, Si/Ca, Si/Na, and Si/K. Figure 27 shows that the Si/Fe ratio of the BSE could be changed by vaporization and atmospheric loss, but the complete mass balance for iron also requires consideration of Earth's core.

We now find which values of $F_g = (1 - F_{\mathrm{BSE}})$ satisfy Equation (64) as a function of temperature for the 270 and 1100 bar steam atmospheres. The intersection of each curve with the horizontal line in Figure 26 gives the maximum temperature at which atmospheric loss from the 270 or 1100 bar steam atmosphere will lower Earth's Si/Mg ratio. These upper temperature limits are $\sim 2590\,\mathrm{K}$ for the 270 bar steam atmosphere and $\sim 2920\,\mathrm{K}$ for the 1100 bar steam atmosphere.
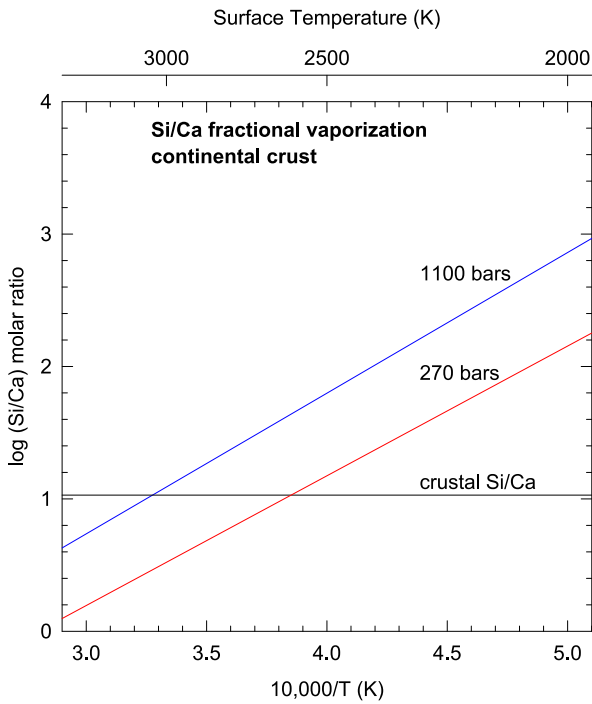
Figure 28. Fractional vaporization of Si and Ca from CC magma (Table 2) into 270 bar (red) and 1100 bar (blue) steam atmospheres as a function of temperature. The Si/Ca ratio in the CC magma is the horizontal black line. The atmospheric Si/Ca ratio is greater than that in the CC above the horizontal line and less than that in the CC below the horizontal line. Thus, atmospheric loss will either deplete (cooler surface temperature) or enrich (hotter surface temperature) the residual rocky planet in Si relative to Ca. The crossover temperature depends on pressure of the steam atmosphere.

Table 5 and Equation (63) give the appropriate k_D values for each case.

At 270 bars and 2000 K, loss of a steam atmosphere having ~1.3% of the mass of the BSE reproduces the CI-normalized Si/Mg ratio (0.854 vs. 0.853). These conditions correspond to a fully molten magma ocean 30° above its liquidus temperature of ~1970 K and a steam atmosphere that can be produced by vaporizing Earth's oceans. The atmospheric mass fraction that needs to be lost to match the Si/Mg ratio decreases slightly with decreasing temperature. It increases proportional to pressure (because $Si(OH)_4$ gas composes ~100% of gaseous silicon, and its mole fraction is proportional to pressure, as shown in Equation (22) and discussed in Sections 5.2.1 and 7.3).

For example, at 270 bars F_g decreases to ~1.2% at 1970 K. Figure 15 shows that the steam atmospheres equilibrated with the BSE are ~75% H_2O by *mass*, so F_g of 1%–1.2% corresponds to losing ~7–8 times Earth's present water inventory (0.107% of the BSE by mass). But at 1100 bars and 2000 K loss of a steam atmosphere having ~5.5% of the BSE mass—or nearly 40 times present Earth's water inventory—is required to match the Si/Mg ratio.

As noted by the referee, correlated depletions due to the enhanced volatility of otherwise refractory elements in a steam atmosphere may lead to characteristic signatures not produced by vaporization from volatile-free magmas (i.e., different from those found by Fegley & Cameron 1987; Leger et al. 2011; Ito et al. 2015). We computed CI-normalized ratios for other important lithophile elements under the same conditions as those discussed above for the Si/Mg ratio (i.e., 2000 K, 270

Table 5
Gas/Magma Molar Distribution Coefficients for Rocky Elements (log D)[a]

Element	2000	2200	2400	2600	2800	3000
	BSE 270 bar Steam Atmosphere					
Si	−5.332	−5.229	−5.199	−5.268	−5.334	−5.400
Mg	−6.967	−6.319	−5.729	−5.205	−4.758	−4.347
Fe	−5.443	−5.061	−4.727	−4.441	−4.197	−3.984
Na	−3.116	−2.950	−2.806	−2.673	−2.541	−2.405
K	−2.607	−2.440	−2.295	−2.158	−2.023	−1.889
Al	−6.023	−5.584	−5.250	−5.030	−4.835	−4.667
Ca	−7.046	−6.415	−5.862	−5.377	−4.949	−4.569
Ni	−5.416	−4.870	−4.451	−4.090	−3.772	−3.491
	BSE 1100 bar Steam Atmosphere					
Si	−4.692	−4.609	−4.550	−4.509	−4.482	−4.465
Mg	−6.989	−6.316	−5.712	−5.187	−4.734	−4.340
Fe	−5.400	−5.015	−4.687	−4.409	−4.173	−3.971
Na	−3.450	−3.278	−3.127	−2.988	−2.854	−2.721
K	−2.909	−2.732	−2.576	−2.432	−2.294	−2.158
Al	−5.721	−5.276	−4.941	−4.722	−4.538	−4.384
Ca	−7.012	−6.370	−5.815	−5.329	−4.902	−4.531
Ni	−5.444	−4.927	−4.539	−4.206	−3.913	−3.652
	Continental Crust 270 bar Steam Atmosphere					
Si	−4.661	−4.562	−4.481	−4.419	−4.364	−4.292
Mg	−5.188	−4.761	−4.367	−3.992	−3.791	−3.691
Fe	−4.108	−3.953	−3.765	−3.570	−3.381	−3.208
Na	−2.695	−2.530	−2.393	−2.279	−2.174	−2.075
K	−3.271	−3.089	−2.940	−2.811	−2.693	−2.580
Al	−5.136	−4.844	−4.592	−4.427	−4.278	−4.144
Ca	−5.766	−5.256	−4.814	−4.425	−4.079	−3.774
Ni	−4.258	−3.950	−3.692	−3.426	−3.154	−2.885
	Continental Crust 1100 bar Steam Atmosphere					
Si	−4.000	−3.913	−3.837	−3.775	−3.729	−3.697
Mg	−5.320	−4.822	−4.354	−3.975	−3.618	−3.287
Fe	−4.084	−3.926	−3.734	−3.545	−3.363	−3.200
Na	−3.284	−3.110	−2.963	−2.844	−2.737	−2.639
K	−3.576	−3.376	−3.212	−3.078	−3.024	−2.845
Al	−5.057	−4.639	−4.284	−4.120	−3.974	−3.849
Ca	−5.816	−5.276	−4.791	−4.396	−4.047	−3.740
Ni	−4.227	−3.912	−3.661	−3.416	−3.178	−2.953

Note.
[a] D = (moles in gas)/(moles in magma).

bars, $F_g = 0.013$). The calculated ratios of Si/Ca (0.852) and Si/Al (0.880) are ~20% larger than the observed ratios of Si/Ca (0.730) and Si/Al (0.720). Calcium and aluminum have about the same depletion factor in the BSE, and it is important that Ca and Al are more volatile than Mg in the steam atmosphere. This is the opposite of their behavior in a solar composition gas, where Al is about as refractory as Ca, and both are more refractory than Mg. It is also the opposite of their behavior for vaporization of anhydrous magmas, where Al and Ca are also more refractory than Mg and remain in the residual magma after evaporative loss (e.g., Figure 6 of Fegley & Cameron 1987; Figure 5 of Leger et al. 2011).

Likewise, the calculated CI-normalized Si/Na (1.4) and Si/K (3.8) ratios produced by vaporization into and subsequent loss of a steam atmosphere are also of the same size as the observed ratios of Si/Na (3.9) and Si/K (4.2) if the k_D values for the halogen-free system are used (Figure 25(a)). However, the loss of Na and K can be 10–20 times higher if we use k_D values for the system with evaporation of alkali hydroxides and halides. We did not estimate the potential loss for Fe with a steam atmosphere because the Fe in the source composition will also distribute between the BSE and the core, which makes

the modeling very complex. These preliminary calculations show that it is possible to match the Si/Mg ratio in the BSE, but more detailed modeling is required to determine the optimal conditions (P, T, mass fraction lost) that give the best match to the observed ratios of lithophile elements in the BSE. This is beyond the scope of this paper and will be done elsewhere.

A larger water inventory on the early Earth is plausible because the chondritic building blocks of Earth contain more H_2O than the present-day Earth. Lodders (2003) gives ∼2.1% H by mass in CI chondrites, which corresponds to ∼18.8% H_2O. This is ∼175 times more water than in the BSE today. On average, other types of chondritic material (i.e., carbonaceous, enstatite, and ordinary) also contain several times more water than Earth (Figure 2 of Fegley & Schaefer 2014). Geochemical models postulating extensive volatile loss from early Earth date back at least to Ringwood (1966). Hydrodynamic escape is a possible mechanism that has been explored with emphasis on noble gases (e.g., Section 6.2 of Porcelli & Pepin 2000 and references therein).

Our calculations for the 270 and 1100 bar steam atmospheres show that fractional vaporization and subsequent loss of rocky elements in a steam atmosphere can explain Earth's Si/Mg ratio and give upper limits for atmospheric mass loss because some of the "missing" Si may have dissolved in Earth's core.

Recent work (e.g., Lopez et al. 2012; Lopez & Fortney 2013, 2014; Kurosaki et al. 2014) indicates that stellar UV-driven mass loss is important for the evolution of hot rocky exoplanets. Detailed modeling of photoevaporative atmospheric loss is beyond the scope of our paper, but we do briefly consider stellar UV photolysis of Fe, Mg, and Si hydroxide gases.

7.6. Photodissociation of Fe(OH)$_2$, Mg(OH)$_2$, and Si(OH)$_4$

The geometries of the three molecules were first optimized using the range-separated CAM-B3LYP functional (Yanai et al. 2004) and the 6-311+g(2 d, p) basis set within the Gaussian 09 suite of programs (Frisch et al. 2009). Figure 29 illustrates the ground-state geometries of the molecules. The energies and transition oscillator strengths for vertical transitions to the first 30 excited states were then computed using the time-dependent (TD) density functional method (Scalmani et al. 2006). The long-range correction in the CAM-B3LYP functional makes it suitable for modeling electron excitations to high-lying orbitals. We have found that for small metal-containing molecules such as AlO, MgCl, NaOH, and SiO, where experimental data are available for comparison, the TD/CAM-B3LYP theory is much better than the Hartree–Fock (HF) theory followed by configuration interaction singles with perturbative doubles correction CIS(D) for excited states, which is a widely used alternative approach (Frisch et al. 2009).

Figure 30 illustrates the calculated photolysis cross section as a function of wavelength ($\sigma(\lambda)$) for the three species. Their photodissociation coefficients (J) were then computed from the relation

$$J_1 = \int_{\lambda_1}^{\lambda_2} \sigma(\lambda)\Phi(\lambda)d\lambda, \qquad (65)$$

where $\Phi(\lambda)$ is the stellar actinic flux at 1 AU (taken as the solar value), and the integration is from the thermodynamic threshold (indicated by arrows in Figure 30) to 120 nm. The resulting J_1 values, for the top of the atmosphere for a solar flux at 1 AU,
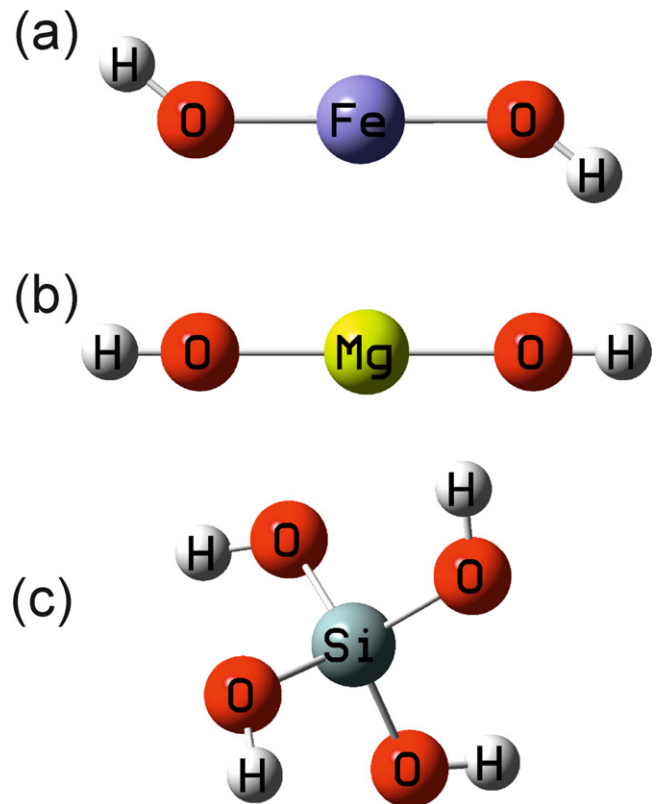
Figure 29. Optimized geometries at the CAM-B3LYP/6-311+g(2d, p) level of theory. Scale: the Fe–O bond length in Fe(OH)$_2$ is 1.77 Å.
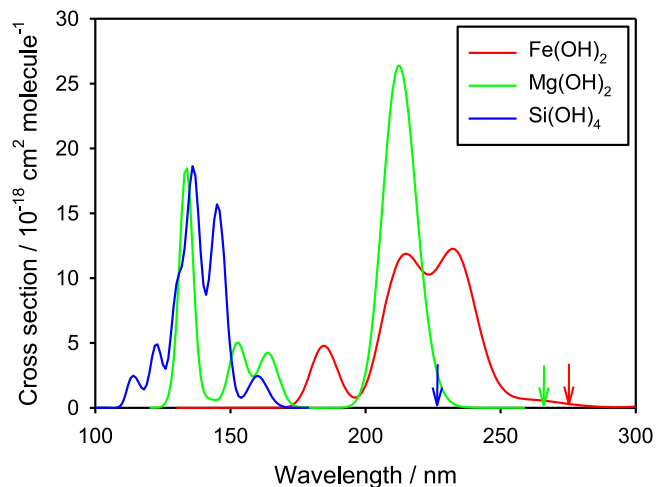
Figure 30. Calculated absorption cross sections as a function of wavelength for Fe(OH)$_2$ (red line), Mg(OH)$_2$ (green line), and Si(OH)$_4$ (blue line). The arrows in corresponding colors indicate the thermodynamic threshold for photolysis.

are listed in Table 6. These values are plausibly upper limits because they neglect the UV opacity of the steam atmosphere. A comparison of the J_1 values in Table 6 and in Table 4 of Schaefer et al. (2012) shows that Fe(OH)$_2$ and Mg(OH)$_2$ are about as photochemically labile as H_2S ($J_1 \sim 3.3 \times 10^{-3}$) and that Si(OH)$_4$ is about as labile as O_2 ($J_1 \sim 4.86 \times 10^{-6}$). The "true" photochemical lifetimes for Si(OH)$_4$, Mg(OH)$_2$, and Fe(OH)$_2$ are expected to be much longer because of the absorption and scattering by other gases (e.g., H_2O, CO_2, SO_2, O_2) in the steam atmospheres.

Table 6
Photodissociation Coefficients for $Fe(OH)_2$, $Mg(OH)_2$, and $Si(OH)_4$

| Reaction	ΔH^{ϕ}_{0K} kJ mol^{-1}	$\lambda_{threshold}$ nm	J s^{-1}
$Fe(OH)_2 + h\nu \rightarrow FeOH + OH$	435	275	2.3×10^{-3}
$Mg(OH)_2 + h\nu \rightarrow MgOH + OH$	450	266	1.3×10^{-3}
$Si(OH)_4 + h\nu \rightarrow Si(OH)_3 + OH$	529	226	4.4×10^{-6}

The photolysis products may be easier to observe than the parental metal hydroxide (M–OH) gases for several reasons. The vibrational frequencies for M–OH bonds lie in the far-infrared, e.g., Spinar & Margrave (1958) observed the strongest absorption at 22.7–23.1 μm in the saturated vapor over NaOH (liquid). Belton & Jordan (1967) estimated the M–OH bending in $Fe(OH)_2$ at ~8.55 μm, and the estimated wavelengths for $Ca(OH)_2$, $Mg(OH)_2$, $Ni(OH)_2$, $Al(OH)_3$, and $Si(OH)_4$ are similar (e.g., see Allendorf et al. 1995; Gurvich et al. 1989; Chase 1999). The O–H stretching frequencies in metal hydroxide gases are estimated to be in the same region as those in water vapor (~2.7–2.8 μm) and are probably masked by water bands in steam atmospheres. On the other hand, Mg, Na, and Si^{2+} are observed escaping from the hot Jupiter HD 209458b (Vidal-Madjar et al. 2013 and references therein), and these gases may also be observable on hot rocky exoplanets with steam atmospheres. Another reason is that the photochemical equilibrium abundances of the metal hydroxide gases may be small compared to the abundances of their photoproducts. We suggest that Al, Ca, Fe, Mg, Ni, and Si (and/or their ions) may be easier to see than the parental metal hydroxide gases. More detailed modeling is beyond the scope of this paper and is not discussed here.

8. POSSIBLE COSMOCHEMICAL APPLICATIONS OF OUR WORK

Our work on rocky element solubility in steam is potentially relevant to several other problems, including the chemistry of Uranus- and Neptune-like exoplanets (mentioned earlier in Section 5.1), chemistry during formation of Earth and the Moon (e.g., B. Fegley et al. 2016, in preparation), transport and fractionation of elements on initially hydrous primitive bodies such as asteroids during heating (e.g., by ^{26}Al), and alkali loss from oxidized, alkali-poor basaltic asteroids such as the parent bodies for the angrite and eucrite meteorites.

The DAWN mission confirmed that the asteroid 4 Vesta is very likely the parent body for eucrites (e.g., see Consolmagno et al. 2015 and references therein), while the angrite parent body is not yet identified. However, in both cases the basaltic meteorites are severely depleted in sodium, with average Na/Al mass ratios of ~0.05 (eucrites) and ~0.003 (angrites), which is only ~8% (eucrites) and ~0.5% (angrites) of the CI-chondritic Na/Al ratio of ~0.6 (CI, Lodders 2003; eucrites, Kitts & Lodders 1998; angrites, Keil 2012). The other alkalies (K, Rb, Cs) are also severely depleted relative to CI-chondritic abundances (Mittlefehldt 1987). The ideas to explain the alkali depletions on the eucrite parent body (EPB = 4 Vesta) include formation of the EPB from volatile-depleted material or loss of volatiles later in the history of the EPB. Lodders (1994) briefly considered thermal escape of alkali hydroxides from the EPB and gave the sequence CsOH

(most volatile) > RbOH > KOH > NaOH > LiOH (least volatile). Vaporization and loss of alkalies from a steam atmosphere on the angrite and eucrite parent bodies may occur under conditions similar to those that oxidize iron, e.g., via the schematic reaction

$$Fe(metal) + H_2O(steam) = \text{“FeO”} + H_2(gas). \qquad (66)$$
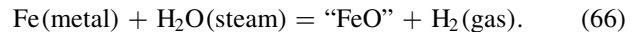
The angrites and eucrites are FeO-rich, with ~18% (eucrites) and ~20% FeO (angrites). Our modeling could be used to study chemistry on the angrite and eucrite parent bodies as noted by the referee.

9. SUMMARY

The major conclusion of our work is that the bulk composition, density, heat balance, and interior structure of rocky planets that are undergoing or have undergone escape of steam-bearing atmospheres may be significantly altered by fractional vaporization and subsequent loss of rocky elements such as Si, Mg, Fe, Ni, Al, Ca, Na, and K that are soluble in steam. In other words, atmospheric loss may alter the composition of the rocky planet left behind if rock dissolves in the atmosphere as is true for rock in steam. This conclusion is based on chemical equilibrium calculations that show rocky element solubility in pure steam and "steam" atmospheres equilibrated with silicate magmas as a function of P, T, and composition.

The chemical equilibrium calculations use tabulated thermodynamic data for hydroxide gases of rocky elements ($Si(OH)_4$, $Mg(OH)_2$, $Fe(OH)_2$, $Ca(OH)_2$, $Al(OH)_3$, and $Ni(OH)_2$) from JANAF and elsewhere (e.g., Plyasunov 2011b, 2012). In turn, the hydroxide gas thermodynamic data are based on extensive experimental studies of the solubility of the major rock-forming elements (e.g., Si, Mg, Fe, Ca, Al, Na, K) in steam. We also show that halide and mixed halide–hydroxide gases of Na, K, Ca, and Al contribute significantly to the solubility of these elements in steam atmospheres. Our conclusions are potentially testable by measurements of planetary mass and radius and *possibly* by spectroscopic observations of the metal hydroxide gases and/or their photolysis products.

between steam atmospheres and magma oceans and its possible effects for planetary compositions.

REFERENCES

Abe, Y. 1993, Litho, 30, 223
Abe, Y., & Matsui, T. 1985, in Proc. 15th Lunar Planet. Sci. Conf., 90, C545
Abe, Y., & Matsui, T. 1988, JAtS, 45, 3081
Ackermann, R. J., Rauh, E. G., Thorn, R. J., & Cannon, M. C. 1963, JPhCh, 67, 762
Akinfiev, N. N., & Plyasunov, A. V. 2013, Fluid Phase Equil., 338, 232
Alexander, C. A., Ogden, J. S., & Levy, A. 1963, JChPh, 39, 3057
Allendorf, M. D., Melius, C. F., Ho, P., & Zachariah, M. R. 1995, JPhCh, 99, 15285
Anderson, G. M., & Burnham, C. W. 1965, AmJS, 263, 494
Antignano, A., & Manning, C. E. 2008, ChGeo, 255, 283
Arrhenius, G., De, B. R., & Alfvén, H. 1974, in The Sea, Vol. 5, ed. E. D. Goldberg (New York: Wiley-Interscience), 839
Bakker, R. J. 2009, Geofluids, 9, 63
Bale, C. W., Chartrand, P., Degterov, S. A., et al. 2002, CALPHAD, 26, 189
Belton, G. R., & Jordan, A. S. 1967, JPhCh, 71, 4114
Belton, G. R., & Richardson, F. D. 1962, Trans. Faraday Soc., 58, 1562
Berman, R. G. 1988, JPet, 29, 445
Berta-Thompson, Z. K., Irwin, J., Charbonneau, D., et al. 2015, Natur, 527, 204
Bézos, A., & Humler, E. 2005, GeCoA, 69, 711
Blander, M., & Pelton, A. D. 1984, in 2nd Int. Symp. on Metallurgical Slags and Fluxes, ed. H. A. Fine, & D. R. Gaskell (New York: Metallurgical Society of AIME), 295
Blumenthal, R. N., & Whitmore, D. H. 1961, JACS, 44, 508
Bockris, J. O'M., Kitchener, J. A., & Davies, A. E. 1952a, Trans Far Soc, 48, 536
Bockris, J. O'M., Kitchener, J. A., Ignatowicz, S., & Tomlinson, J. W. 1948, Far Soc Disc, 4, 265
Bockris, J. O'M., Kitchener, J. A., Ignatowicz, S., & Tomlinson, J. W. 1952b, Trans Far Soc, 48, 75
Brady, E. L. 1953, JPhCh, 57, 706
Brewer, L., & Mastick, D. F. 1951, JChPh, 19, 834
Bureau, H., & Keppler, H. 1999, E&PSL, 165, 187
Canil, D., O'Neill, H. St. C., Pearson, D. G., et al. 1994, E&PSL, 123, 205
Carmichael, I. S. E., Nicholls, J., Spera, F. J., et al. 1977, RSPTA, A286, 373
Chase, M. W. 1998, in, J. Phys. Chem. Ref. Data Monograph, Vol. 9, NIST-JANAF Thermochemical Tables, (4th ed.; Washington, DC: ACS and Melville, NY: AIP)
Chervonnyi, A. D., Piven, V. A., Kashireninov, O. E., & Manelis, G. B. 1977, HTemS, 9, 99
Chizikov, D. M., Tsvetkov, Y. V., & Kazenas, E. K. 1971, Metally, 3, 55
Claire, M. W., Catling, D. C., & Zahnle, K. J. 2006, Geobiology, 4, 239
Consolmagno, G. J., Golabek, G. J., Turrini, D., et al. 2015, Icar, 254, 190
Cruz, M. F., & Manning, C. E. 2015, CoMP, 170, 35
Dressing, C., Charbonneau, D., Dumusque, X., et al. 2015, ApJ, 800, 135
Drowart, J., DeMaria, G., Burns, R. P., & Inghram, M. G. 1960, JChPh, 32, 1366
Elkins-Tanton, L. 2008, E&PSL, 271, 181
Elliot, G. R. B. 1952, PhD thesis, University of California, Berkley
Farber, M. S., Harris, S. P., & Srivastava, R. D. 1974, CoFl, 22, 191
Fegley, B., Jr. 2013, Practical Chemical Thermodynamics for Geoscientists (Amsterdam: Elsevier)
Fegley, B., Jr. 2014, Goldschmidt Abstracts, 2014, 675
Fegley, B., Jr., & Cameron, A. G. W. 1987, E&PSL, 82, 207
Fegley, B., Jr., & Prinn, R. G. 1986, ApJ, 307, 852
Fegley, B., Jr., & Schaefer, L. 2014, in Treatise on Geochemistry, ed. H. D. Holland, & K. K. Turekian (Amsterdam: Elsevier), 71
Fei, Y. 1995, in Global Earth Physics: A Handbook of Physical Constants, ed. T. Ahrens (Washington, DC: AGU), 29
Fournier, R. O., & Potter, R. W., II 1982, GeCoA, 46, 1969
Frisch, M. J., et al. 2009, Gaussian 09, Revision A.1 (Wallingford, CT: Gaussian, Inc.)
Fyfe, W. S., & Hollander, M. A. 1964, AmJS, 262, 709
Gerya, T. V., Maresch, W. V., Burchard, M., et al. 2005, Eur. J. Mineral., 17, 269
Gettel, S., Charbonneau, D., Dressing, C. D., Buchhave, L. A., & Dumusque, X. 2015, ApJ, in press (arXiv:1511.09097)
Ghiorso, M. S., & Carmichael, I. S. E. 1980, CoMP, 71, 323
Ghiorso, M. S., Hirschmann, M. M., Riners, P. W., & Kress, V. C., III 2002, GGG, 3, 5
Ghiorso, M. S., & Sack, R. O. 1995, CoMP, 119, 197

Goranson, R. W. 1932, AmJS, 23, 227
Green, D. H. 2015, PCM, 42, 95
Grimley, R. T., Burns, R. P., & Ingrham, M. G. 1961, JChPh, 35, 551
Gualda, G. A. R., Ghiorso, M. S., Lemons, R. V., & Carley, T. L. 2012, JPet, 53, 875
Gunnarsson, I., & Arnórsson, S. 2000, GeCoA, 64, 2295
Gurvich, L. V., Iorish, V. S., Chekhovskoi, D. V., & Yungman, V. S. 1983, IVTANTHERMO–A Thermodynamic Database and Software System for the Personal Computer, NIST Special Database 5
Gurvich, L. V., Veyts, I. V., & Alcock, C. B. 1989, Thermodynamic Properties of Individual Substances, Vol. 1 (1989), Vol. 2 (1991), Vol. 3 (1994) (Boca Raton, FL: CRC Press)
Haas, H. 1972, AmMin, 57, 1375
Hamano, K., Abe, Y., & Genda, H. 2013, Natur, 497, 607
Hamano, K., Kawahara, H., Abe, Y., Onishi, M., & Hashimoto, G. L. 2015, arXiv:1505.03552
Hashimoto, A. 1992, GeCoA, 56, 511
Hastie, J. W. 1975, High Temperature Vapors (New York: Academic)
Hastie, J. W., Bonnell, D. W., & Schenk, P. K. 2000, Pure Appl Chem, 72, 2111
Hemingway, B. S. 1990, AmMin, 75, 781
Hemingway, B. S., Bohlen, S. R., Hankins, W. B., Westrum, E. F., Jr., & Kuskov, O. L. 1998, AmMin, 83, 409
Hildenbrand, D. L., & Lau, K. H. 1994a, JChPh, 101, 6076
Hildenbrand, D. L., & Lau, K. H. 1994b, JChPh, 108, 6535
Hirschmann, M. M., & Dasgupta, R. 2009, ChGeo, 262, 4
Holland, T. J. B., & Powell, R. 2011, J. Met. Geol., 29, 333
Holzheid, A., Palme, H., & Chakraborty, S. 1997, ChGeo, 139, 21
Hunt, J. D., & Manning, C. E. 2012, GeCoA, 86, 196
Hunten, D. M., Pepin, R. O., & Walker, J. C. G. 1987, Icar, 69, 532
Ito, Y., Ikoma, M., Kalahari, H., Nagahara, H., Kawashima, Y., & Nakamoto, T. 2015, ApJ, 801, 144
Jacobson, N. S., Opila, E. J., Myers., D. L., & Copland, E. H. 2005, J. Chem. Thermo., 37, 1130
Jacobsson, E 1985, Scand J Met, 14, 252
Jennings, E. S., & Holland, T. J. B. 2015, JPet, 56, 869
Kargel, J. S., & Lewis, J. S. 1993, Icar, 105, 1
Kazenas, E. K., Samoilova, I. O, & Zviadadze, G. N. 1983, RJPCA, 57, 1571
Kazenas, E. K., & Tagirov, V. K. 1995, Metally, 2, 27
Kazenas, E. K., Zviadadze, G. N., & Bol'shikh, M. A. 1985, Metally, 1, 46
Keil, K. 2012, ChEG, 72, 191
Kennedy, G. C. 1950, Econ. Geol., 45, 629
Kennedy, G. C. 1956, AmJS, 254, 567
Kennedy, G. C. 1959, AmJS, 257, 563
Kennedy, G. C., Wasserburg, G. J., Heard, H. C., & Newton, R. C. 1962, AmJS, 260, 501
Kitahara, S. 1960, Rev Phys Chem Japan, 30, 109
Kite, E. S., Fegley, B., Jr., Schaefer, L., & Gaidos, E. 2016, ApJ, submitted
Kitts, K., & Lodders, K. 1998, M&PS, 33, A197
Korzhinskii, D. S. 1959, Physicochemical Basis of the Analysis of the Paragenesis of Minerals (New York: Consultants Bureau)
Krieger, F. J. 1965, Rand Corporation Memorandum RM-4804-PR
Krieger, F. J. 1966a, Rand Corporation Memorandum RM-4943-PR
Krieger, F. J. 1966b, Rand Corporation Memorandum RM-5042-PR
Krieger, F. J. 1967, Rand Corporation Memorandum RM-5248-PR
Krikorian, O. H. 1970, in Symp. on Engineering with Nuclear Explosives, 1, 481
Kurosaki, K., Ikoma, M., & Hori, Y. 2014, A&A, 562, A80
Kushiro, I., Syono, Y., & Akimoto, S. I. 1968, JGR, 73, 6023
Kuts, S. M. 1967, Teplo, 14, 120
Lange, M. A., & Ahrens, T. J. 1982, Icar, 51, 96
LeBrun, T., Massol, H., Chassefiere, E., et al. 2013, JGR, 118, 1155
Leger, A., Grasset, O., Fegley, B., et al. 2011, Icar, 213, 1
Linard, Y., Nonnet, H., & Advocat, T. 2008, JNCS, 354, 4917
Lodders, K. 1994, MAPS, 29, 492
Lodders, K. 2003, ApJ, 591, 1220
Lodders, K., & Fegley, B., Jr. 1998, The Planetary Scientist's Companion (New York: Oxford Univ. Press)
Lodders, K., Palme, H., & Gail, H. P. 2009, in Landolt-Börnstein, New Series, Vol. VI/B, ed. J. E. Thünper (Berlin: Springer), 560
Lopez, E. D., & Fortney, J. J. 2013, ApJ, 776, 2
Lopez, E. D., & Fortney, J. J. 2014, ApJ, 792, 1
Lopez, E. D., Fortney, J. J., & Miller, N. 2012, ApJ, 761, 59
Maeda, E., Sasomoto, T., & Sata, T. 1978, Yogyo-Kyokai-Shi, 86, 492
Manning, C. E. 1994, GeCoA, 58, 4831
Matsui, T., & Abe, Y. 1986, Natur, 322, 526

Matsumoto, K., & Sata, T. 1981, Bull Chem Soc Japan, 54, 674
Melosh, H. J. 2007, MAPS, 42, 2079
Meschter, P. J., Opila, E. J., & Jacobson, N. S. 2013, AnRMS, 3, 559
Mittlefehldt, D. W. 1987, GeCoA, 51, 267
Morey, G. W. 1957, Econ. Geol., 52, 225
Morey, G. W., Fournier, R. O., & Rowe, J. J. 1962, GeCoA, 26, 1029
Morey, G. W., & Hesselgesser, J. M. 1951a, Econ. Geol., 46, 821
Morey, G. W., & Hesselgesser, J. M. 1951b, Trans AIME, 73, 865
Mosebach, R. 1957, JG, 65, 347
Motalebi, F., Udry, S., Gillon, M., et al. 2015, A&A, 584, A72
Muan, A., & Osborn, E. F. 1965, Phase Equilibria among Oxides in
    Steelmaking (Reading, MA: Addison-Wesley)
Newton, R. C., & Manning, C. E. 2002, GeCoA, 66, 4165
Newton, R. C., & Manning, C. E. 2003, CoMP, 146, 135
Newton, R. C., & Manning, C. E. 2008, E&PSL, 274, 241
Nguyen, Q. N., Myers, D. L., Jacobson, N. S., & Opila, E. J. 2014, NASA/
    TM-2014-218372
Nittler, L. R., Starr, R. D., Wider, S. Z., et al. 2011, Sci, 333, 1847
O'Neill, H. St. C. 1988, AmMin, 73, 470
O'Neill, H. St. C., & Pownceby, M. I. 1993, CoMP, 114, 296
Opila, E. J., Fox, D. S., & Jacobson, N. S. 1997, JACS, 80, 1009
Opila, E. J., & Myers, D. L. 2004, JACS, 87, 1701
O'Rourke, J. G., & Stevenson, D. J. 2016, Natur, 529, 287
Palme, H., & O'Neill, H. S. C. 2014, Cosmochemical Estimates of Mantle
    Composition. Treatise on Geochemistry (2nd ed.; Amsterdam: Elsevier)
Pawley, A. R., Redfern, S. A. T., & Holland, T. J. B. 1996, AmMin, 81, 335
Pelton, A. D., & Blander, M. 1984, in 2nd Int. Symp. on Metallurgical Slags
    and Fluxes, ed. H. A. Fine, & D. R. Gaskell (New York: Metallurgical
    Society of AIME), 281
Pepin, R. O. 1997, Icar, 126, 148
Perkins, D., III, Essene, E. J., Westrum, E. F., Jr., & Wall, V. J. 1979, AmMin,
    64, 1080
Pitzer, K. S., & Brewer, L. 1961, Thermodynamics (2nd ed.; New York:
    McGraw-Hill)
Plyasunov, A. V. 2011a, Fluid Phase Equil, 305, 212
Plyasunov, A. V. 2011b, GeCoA, 75, 3853
Plyasunov, A. V. 2012, GeCoA, 77, 215
Porcelli, D., & Pepin, R. O. 2000, in Origin of the Earth and Moon, ed.
    R. M. Canup, & K. Righter (Tucson: University of Arizona Press), 435
Powell, R., Holland, T. J. B., & Worley, B. 1998, J Met Geol, 16, 577
Preston, E., & Turner, W. E. S. 1934, J Soc. Glass Tech., 18, 222
Rimstidt, J. D. 1997, GeCoA, 61, 2553
Ringwood, A. E. 1966, GeCoA, 30, 41
Robie, R. A., & Hemingway, B. S. 1995, USGS Bulletin, 2131
Rollason, R. J., & Plane, J. M. C. 2000, PCCP, 2, 2335
Rowlinson, J. S., & Swinton, F. L. 1982, Liquids and Liquid Mixtures (3rd ed.;
    London: Butterworths)
Saal, A. E., Hauri, E. H., Langmuir, C. H., & Perfit, M. R. 2002, Natur,
    419, 451

Salmon, O. N. 1961, JPhCh, 65, 550
Samoilova, I. O., & Kazenas, E. K. 1995, Metally, #1, 33
Scalmani, G., Frisch, M. J., Mennucci, B., et al. 2006, JChPh, 124,
    094107
Schaefer, L., & Fegley, B., Jr. 2007, Icar, 186, 462
Schaefer, L., & Fegley, B., Jr. 2009, ApJL, 703, L113
Schaefer, L., & Fegley, B., Jr. 2010, Icar, 205, 483
Schaefer, L., Lodders, K., & Fegley, B. 2012, ApJ, 755, 41
Shchedrin, W. M., Kulikov, I. S., Vas'kin, V. N., & Teleguin, A. A. 1978,
    J Chem Thermo, 10, 9
Shen, A. H., & Keppler, H. 1997, Natur, 385, 710
Sleep, N. H., Zahnle, K., & Neuhoff, P. S. 2001, PNAS, 98, 3666
Spencer, P. J., & Kubaschewski, O. 1978, CALPHAD, 2, 147
Spinar, L. H., & Margrave, J. L. 1958, AcSpe, 12, 244
Straub, F. G., & Grabowski, H. A. 1945, Trans AIME, 67, 309
Symonds, R. B., Rose, W. I., Bluth, G. J. S., & Gerlach, T. M. 1994, in
    Volatiles in Magmas, ed. M. R. Carroll, & J. R. Holloway (Washington,
    DC: Mineralogical Society of America), 1
Takahashi, E. 1986, JGR, 91, B9367
Takahashi, E., Shimazaki, T., Tsuzaki, Y., & Yoshida, H. 1993, RSPTA,
    342, 105
Thompson, J. B. 1981, in Amphiboles and Other Hydrous Pyriboles–
    Mineralogy, ed. D. R. Veblen (MSA), 141
Tossell, J. A. 2005, GeCoA, 69, 283
Tyburczy, J. A., Frisch, B., & Ahrens, T. J. 1986, E&PSL, 80, 201
Van Nieuwenberg, C. J., & Blumendal, H. B. 1930, Rec Trav Aux Chim,
    49, 857
Van Nieuwenberg, C. J., & Blumendal, H. B. 1931a, Rec Trav Aux Chim,
    50, 129
Van Nieuwenberg, C. J., & Blumendal, H. B. 1931b, Rec Trav Aux Chim,
    50, 989
Van Zeggern, F., & Storey, F. H. 1970, The Computation of Chemical
    Equilibria (Cambridge: Cambridge Univ. Press)
Vanderburg, A., Latham, D., Bucchave, L. A., et al. 2015, ApJS, in press
Verhoogen, J. 1949, Thermodynamics of a Magmatic Gas Phase (Vol. 28;
    Berkeley, CA: University of California Press)
Vidal-Madjar, A., Huitson, C. M., Bourrier, V., et al. 2013, A&A,
    560, A54
Wagner, W., & Pruss, A. 2002, JPCRD, 31, 387
Walther, J. V., & Helgeson, H. C. 1977, AmJS, 277, 1315
Warneck, P. 1989, Chemistry of the Natural Atmosphere (San Diego, CA:
    Academic)
Wasserburg, G. J. 1958, JG, 66, 559
Wedepohl, K. H. 1995, GeCoA, 59, 1217
Weill, D. F., & Fyfe, W. S. 1964, GeCoA, 28, 1243
Yanai, T., Tew, D., & Handy, N. 2004, CPL, 393, 51
Yaroshevsky, A. A. 2006, GeocI, 44, 48
Zahnle, K. J., Kasting, J. F., & Pollack, J. B. 1988, Icar, 74, 62
Zotov, N., & Keppler, H. 2002, ChGeo, 184, 71